SELF-PROPELLING ROBOTIC HYDROFOIL ARRAYS: MECHANICS, EFFICIENCY, AND OPTIMIZATION

by

Rakshit Bhansali

A thesis submitted to the faculty of
The University of North Carolina at Charlotte
in partial fulfillment of the requirements
for the degree of Master of Science in
Mechanical Engineering

Charlotte

2018

Approved by:

_____

Dr. Scott David Kelly

_____

Dr. Russell Keanini

_____

Dr. Srinivas Akella

ABSTRACT

RAKSHIT BHANSALI. Self-propelling robotic hydrofoil arrays: mechanics, efficiency, and optimization. (Under the direction of DR. SCOTT DAVID KELLY)

Mathematical models for the self-propulsion of articulated bodies in fluids at low Reynolds number can be interpreted geometrically in terms of connections in principal bundles. Visualization of the local curvature of a connection in this context can serve as a tool for motion planning. We use laboratory data from physical experiments to estimate the local curvatures of connections for two planar robotic systems — one canonical, one novel — propelling themselves through fluids at Reynolds numbers of order one. In each case, the estimated curvature agrees with that predicted by a trusted theoretical model, validating our approach as a new strategy for extracting curvature estimates from physical data when theoretical model are unavailable.

For one of the two robotic systems in question, we also employ reinforcement learning to identify piecewise constant control inputs that optimize unidirectional translation. Our results show that optimal locomotion over long time scales is achieved through cyclic actuation that exploits curvature according to the geometric theory — and that exploits the nontrivial topology of the manifold of internal robot shapes — while optimal locomotion over short times scales requires adaptation for different initial conditions.

We also investigate the self-propulsion of pitching hydrofoils at higher Reynolds numbers through physical experiments with freely swimming two- and four-hydrofoil arrays, resembling simplified fish schools, in a pool of water. These experiments highlight the influence of hydrodynamic coupling among individual foils on the overall speed and efficiency of such arrays. We modulate this coupling by varying the spacing among foils and by varying the manner in which individual foils pitch as functions of time, recording both swimming speed and power consumption to identify optimal

cooperative pitching patterns.

ACKNOWLEDGEMENTS

First and foremost, I would like to thank Dr. Scott Kelly for his immeasurable guidance and support throughout my duration at UNC Charlotte. I would also like to thank Dr. Russell Keanini and Dr. Srinivas Akella for being a part of my thesis committee and reviewing my thesis.

A special thanks to my colleague and friend, Rodrigo Abrajan Guerrero, for sharing his intellect and encouragement. A kind mention to Dr. Michael Fairchild for sharing some of his ideas. My thanks goes out to all my friends especially Blake Buchanan and Hunter Soper for their valuable inputs and help with some of the setup; Omkar Aradhye, Pratik Ghag, Ashwin Ananthapadmanabhan and others for their support during the course of this project. Lastly, my gratitude to my mother and other family members who have always shown faith in me and stood by me through difficult times.

TABLE OF CONTENTS

LIST OF FIGURES

CHAPTER 1: INTRODUCTION

We marvel at the sight of the lightning fast sprint of a cheetah, the impulsive agility of a marlin, the harmonic undulation of a snake and the impressive leap of a grasshopper. All these animals select gaits based on speed, terrain, maneuvers and energy efficiency.

The study of animal locomotion was limited before the 19^{th} century. It was not until the invention of motion-picture projection [3] by Eadweard Muybridge that this field caught traction. Sir James Gray, one of the early pioneers in the study of animal locomotion, used this technique of motion-picture projection to notice the similarities in undulatory body motion of swimming eels and fishes [4]. A few years later, Hoyt et al. [5] discovered that the natural gait of any living organism for any given speed is the one that expends the least energy by validating physical measurements obtained from trained horses. Edward M. Purcell [6] came up with the idea of gait-based motion of an imaginary three-link swimmer at low Reynolds number flows by prescribing cyclic gaits in the shape space.

One of the earliest geometric approaches to locomotion was that of Shapere and Wilczek [7], who studied the problem of swimming at low Reynolds number in terms of gauge theory. They advanced terms like geometric phase and holonomy, which are lately being discussed in robotic motion planning literature, to understand the motion of paramecia. Leading pioneers in the field of geometric mechanics like Murray and Sastry [8] demonstrated the use of sinusoidal gaits for a broad class of two-input systems. Influenced by their work, Kelly [9] showed that in viscous flow regimes, where the inertial effects are nullified by the flow drag, the propulsion of self-deforming solid bodies can be modeled in terms of a connection on a principal fiber bundle.

A well known fact in the field of fluid-solid interactions is that self-deforming solid bodies in close proximity to one another in a fluid medium can influence each other's dynamics. This phenomenon is commonly seen in group formations among bird and fish species where the energy harvested from the vortices in the unsteady wake of each individual's neighbor can be used by the individual to help overcome collective drag. Although there exist assumptive theories to the problem of wake vortex shedding, posing this in terms of a geometric mechanics problem still remains abstruse. The dynamics of vortex generation in fish schools plays a critical role in energy sharing. It is observed that the flapping motion of a fish creates a trail of rotating vortices similar to the arrangement of a von Kármán street but opposite in the direction of rotation. Neighboring fishes can extract energy of each other's wakes by timing their motions to generate counter-rotating vortices that pair-up with the vortices from the neighbor's wake and generate thrust. This phenomenon of vortex interactions is widely described in [10], [11], [12], [13]. The interaction of vortices is heavily reliant on the geometric arrangement of oscillating bodies in the flow. Weihs [14], in 1973, suggested diamond shaped patterns as the optimal arrangement of fishes in a school with the aim of maximizing energy harvesting, given the assumption that the fluid in which they swim is inviscid. Triantafyllou et al. [13] demonstrated the importance of free-wake vorticity in deciding the frequency and form of swimming motion which is beneficial for energy extraction. Researchers like Zhang and Eldredge [15] proposed a high fidelity numerical model called VVPM(Viscous Vortex Particle Method) to solve for the Navier-Stokes equations of the unsteady two-dimensional flow with multiple undulating fish bodies. They claim that the thrust augmentation for a system of two fishes placed laterally with respect to one another were found to be quite monotonic for spacings greater than one bodylength and upto four bodylengths. Kelly et al. [16] demonstrated the effects of hydrodynamic coupling on the propulsive efficiency of an array of three oscillating hydrofoils and made the claim that oppositely-polarized vor-

tices from a pack of adjacent swimmers, when sufficiently close, collide and superpose to cancel one another and increase array efficiency locally. They also highlight the importance of near-field wake interactions to determine propulsive efficiency of the array. Boschitsch et al. [17], Dewey et al. [18] experimentally studied the behavior of vortex shedding with in-line and side-by-side arrangement of oscillating hydrofoils respectively. They made observations about the performance of these systems based on thrust and efficiency and highlight the importance of vortex interactions for performance augmentation.

1.1 Motivation

During the course of this thesis, we focus our attention towards three problems - First, we extract the local curvature of articulated bodies self-propelling in low Reynolds number flows using fundamentals from geometric mechanics. Second, we seek non-cyclic gaits that maximize uni-directional displacement for the former using reinforcement learning. Finally, we identify the optimal placement of hydrofoils/paddles that maximize the effect of energy harvesting through shared medium by comparing thrust and propulsive efficiency for various arrangements of hydrofoils at high Reynolds number flows.

In low Reynolds number flows (Re in the order of one), if the body moves in a time-periodic way, then the net change in position and orientation over one period can be thought of as the geometric phase associated with a closed path in the manifold of body shapes [1]. We propose a procedure that will allow us to estimate the geometric phase by executing cyclic shape changes that enclose curvature when embedded on the manifold of shapes/shape space. We experimentally perform these cyclic shape changes and center them at different locations in the manifold of shapes and record the net displacement/change in orientation after the shape change. The shape change may be done over 1 cycle or n cycles to amplify the net motion. The displacement/change in orientation may be regarded as the group element or holonomy for that loop.

As experiments are performed in all the locations in the discretized shape space, we attach the corresponding holonomy to each location and visually predict the curvature for motion planning.

Although cyclic gaits are well studied analytically to extract the geometric phase, we look for possibilities of finding gaits that can maximize the uni-directional motion of the body using reinforcement learning. *"Reinforcement learning is learning what to do? how to map situations to actions? so as to maximize a numerical reward signal"* [19]. The crucial part of this technique is framing the problem of learning from interaction with the environment by solving the dynamics of the system and reaching a pre-defined goal. The use of RL is widely publicized in automatic control, computer science, artificial intelligence, et cetera.

Finally, we consider multiple hydrofoil systems (akin the systems considered for low Reynolds number flow) at high Reynolds number flow. For the purpose of this thesis, we refer to systems in Reynolds number in the order of 10^4 as high Reynolds number flow systems. We pose this as an optimization problem with the aim of maximizing the propulsive efficiency of the multiple hydrofoil system. We perform experiments with a light reconfigurable robotic setup and deploy it in a free swimming laboratory environment with no background flow. We analyze the data from these experiments and look for pairwise synchronized arrangements that result in efficient system performance. Additionally, to evoke the idea of using intermittent gaits over commonly analyzed sinusoids, we make experimental thrust comparisons between the symmetric and asymmetric gaits and comment on its merits and demerits.

CHAPTER 2: SYSTEMS IN LOW REYNOLDS NUMBER FLOW

In the context of Stokes flow (Re«1), Scallop's theorem states that for a system to propel, it must do so in a way that is not invariant upon time-reversal. This is contradictory to the systems analyzed here where the model we will derive assumes that the locomotion through shape change[1] is driftless [1].

We assume our systems to be planar and define external dimensional spaces on the SE(2) special Euclidean group which we refer to as a matrix Lie group G. Coordinates on the principal bundle's fiber manifold parameterize the body's position and orientation relative to a stationary frame of reference as shown in Figure 2.1. The coordinates on the bundle's base manifold M or the manifold of shape changes parameterize the body's shape. The collection of all possible configurations of the system corresponds to a manifold called the configuration manifold Q and the relationship is shown in Equation 2.1.

$$Q = M \times G \tag{2.1}$$

If the body moves in a time-periodic way, then the net change in position and orientation over one period can be thought of as the geometric phase associated with a closed path in the manifold of body shapes. In the limit as such a path becomes small — that is, if the cyclic change in the body's shape represents only a small perturbation from a nominal shape — then the associated geometric phase can be approximated by exponentiating the integral of a $\mathfrak{g}$-valued two-form called the local curvature over the area enclosed by the path [1].

[1] A shape change is defined as a change in the internal configuration of the system

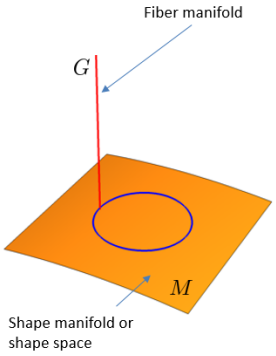

Figure 2.1: Configuration Manifold

The relationship between shape change and propulsion is time-invariant, and reversibility prevents any net displacement or change in orientation from a cyclic deformation that doesn't enclose area in the manifold of shape variables [1].

The first system considered is a variation of the canonical Purcell three-link swimmer as shown in Figure 2.2.

2.1 Purcell swimmer

The Purcell swimmer [6], a hypothetical animal with three links — the side links act as a rudders and the middle link as the body — has been extensively studied both analytically and experimentally in literature. The principal bundle for this system looks like

$$Q = \mathbb{T}^2 \times \mathbb{SE}(2), \tag{2.2}$$

where $\mathbb{T}^2$ is the base manifold comprising of the shape variables ϕ and ψ, and $\mathbb{SE}(2)$ represents the special Euclidean structure group over the base manifold.

We model the local curvature of this self-propelling by analytically reproducing the results from [20] using slender-body theory [21] under the simplifying assumption that the hydrodynamics of each link are decoupled from the hydrodynamics of the others.

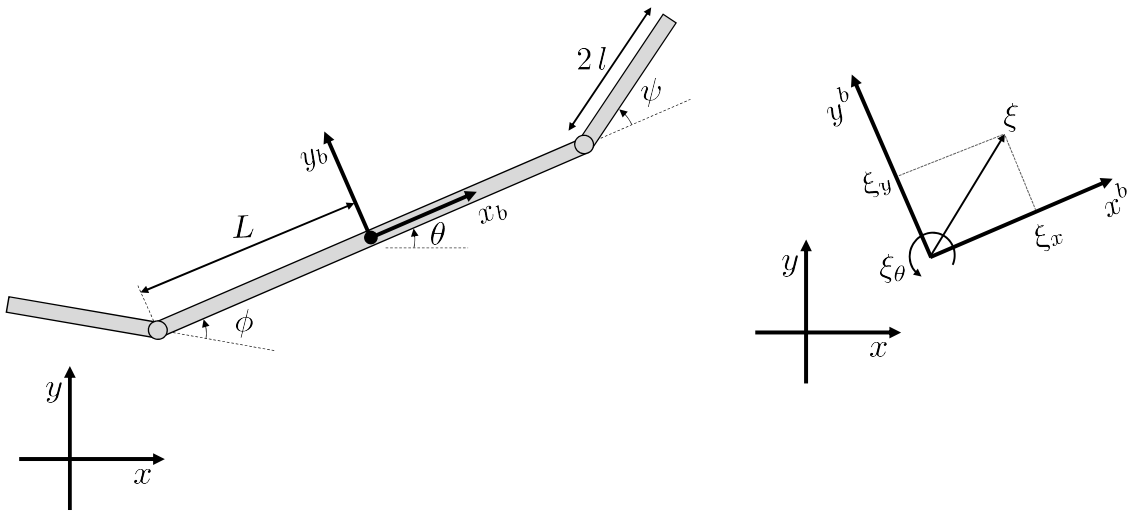

Figure 2.2: Three-link swimmer. *Left*: Model geometry. *Right*: Body velocity [1].

Figure 2.2 depicts the Purcell three-link swimmer where the outer links each have length $2l$ while the middle link has length $2L$, with $L > l$. The joint angles ϕ and ψ are defined as shown.

According to slender-body theory, for low Reynolds number flows, the longitudinal and lateral forces on each link and the moment about the center of each link are given by

$$F_{i,x} = k\, l_i\, \xi_{i,x}, \quad F_{i,y} = 2k\, l_i\, \xi_{i,y}, \quad M_i = \frac{2}{3} k\, l_i^3\, \xi_{i,\theta}, \tag{2.3}$$

respectively, where $\xi_i = [\xi_{i,x}, \xi_{i,y}, \xi_{i,\theta}]^T$ is the body velocity of the ith link, $l_1 = l_3 = l$, $l_2 = L$, and k is a constant. The frame of reference is attached to the center of the middle link, aligning the longitudinal direction with the side-links.

The body velocities are given by

$$\xi_1 = \begin{bmatrix} \cos(\phi)\xi_x - \sin(\phi)\xi_y + L\sin(\phi)\xi_\theta \\ \sin(\phi)\xi_x + \cos(\phi)\xi_y - (l + L\cos(\phi))\xi_\theta + l\dot{\phi} \\ \xi_\theta - \dot{\phi} \end{bmatrix},$$

$$\xi_2 = \xi,$$

$$\xi_3 = \begin{bmatrix} \cos(\psi)\xi_x + \sin(\psi)\xi_y + L\sin(\psi)\xi_\theta \\ -\sin(\psi)\xi_x + \cos(\psi)\xi_y + (l + L\cos(\psi))\xi_\theta + l\dot{\psi} \\ \xi_\theta + \dot{\psi} \end{bmatrix}.$$

Summing forces and moments about the body-fixed frame, we obtain the generalized force vector

$$F = \begin{bmatrix} F_x \\ F_y \\ M \end{bmatrix} = \begin{bmatrix} \cos(\phi) & \sin(\phi) & 0 \\ -\sin(\phi) & \cos(\phi) & 0 \\ L\sin(\phi) & -L\cos(\phi) - l & 1 \end{bmatrix} \begin{bmatrix} F_{1,x} \\ F_{1,y} \\ M_1 \end{bmatrix} + \begin{bmatrix} F_{2,x} \\ F_{2,y} \\ M_2 \end{bmatrix} + \begin{bmatrix} \cos(\psi) & -\sin(\psi) & 0 \\ \sin(\psi) & \cos(\psi) & 0 \\ L\sin(\psi) & L\cos(\psi) + l & 1 \end{bmatrix} \begin{bmatrix} F_{3,x} \\ F_{3,y} \\ M_3 \end{bmatrix}.$$

We can rewrite this in the form

$$F = \omega(s) \begin{bmatrix} \xi \\ \dot{s} \end{bmatrix}, \tag{2.4}$$

where $s = [\phi, \psi]^T$ represents the shape variables and $\omega(s)$ is a 3×5 matrix. Furthermore, we can write

$$\omega(s) = \begin{bmatrix} \omega_1 & \omega_2 \end{bmatrix},$$

where ω_1 and ω_2 are 3×3 and 3×2 matrices respectively.

In an isolated system, the forces and moments must sum to zero[1]; hence we obtain a connection from the requirement that

$$F = \begin{bmatrix} 0 \\ 0 \\ 0 \end{bmatrix} = \begin{bmatrix} \omega_1 & \omega_2 \end{bmatrix} \begin{bmatrix} \xi \\ \dot{s} \end{bmatrix},$$

which can be rearranged into the form

$$\xi = -\omega_1^{-1}\omega_2\dot{s}, \tag{2.5}$$

which has the form of the *kinematic reconstruction equation*,

$$\xi = -A(s)\dot{s}. \tag{2.6}$$

Thus, the local connection is given by $A(s) = \omega_1^{-1}\omega_2$, which shows how the shape velocity vectors translate into body velocities.

The local connection $A(s)$ geometrically encompasses everything we need to know about the system. We approximate for the holonomy (h) — defined as the displacement along the fiber due to a closed loop trajectory (C) in the shape variables — by

$$h \approx \exp\left(-\int_{\text{interior of } C} \mathrm{D}A\right), \tag{2.7}$$

where $\mathrm{D}A$ is a two-form such that

$$\mathrm{D}A(u, v) = \mathrm{d}A(u, v) - [A(u), A(u)], \tag{2.8}$$

with $[\cdot\,,\cdot]$ being the Lie bracket, u and v are the two shape velocity vectors, and $\mathrm{d}A$ is the exterior derivative of A, considering A to be a Lie algebra valued one-form. This $\mathrm{d}A$ is depicted in Figure 2.3 as functions of ϕ and ψ, also known as *curvature plots*.

Knowing what the curvature plot of a system looks like on the manifold of body shapes, one can facilitate a visual approach to motion planning based on the qualitative notion that a path enclosing greater curvature will be a path that produces greater displacement and/or reorientation. It is known that positive (counter-clockwise) closed loops in shape space enclosing positive curvature will generate negative locomotion in their corresponding components, and those enclosing negative curvature will generate positive locomotion with respect to the frame of reference. The response is inverted if the direction of the closed loops are inverted. This locomotion or displacement along the fiber, after executing a closed-loop trajectory, is also known as the holonomy, h.

2.2 Four-paddle swimmer

The second system we consider, depicted in Figure 2.4, consists of four paddles with hinges placed at the corners of a square of side $\sqrt{2}L$. The length of each paddle is $2l$. The paddles are numbered 1 through 4 starting with the top right one and continuing in a counterclockwise direction. The orientations of the paddles are determined by the shape variables ϕ and ψ as indicated in the figure. Paddles 1 and 3 (in red) move in unison as parameterized by ϕ; paddles 2 and 4 (in blue) move in a mirrored way as parameterized by ψ. The frame of reference is attached to the center of the square, aligning the longitudinal direction with the diagonal between paddles 1 and 3. A body frame is considered to be attached at the center of each paddle, with its longitudinal direction aligned with the paddle and the positive direction going away from the hinge[1].

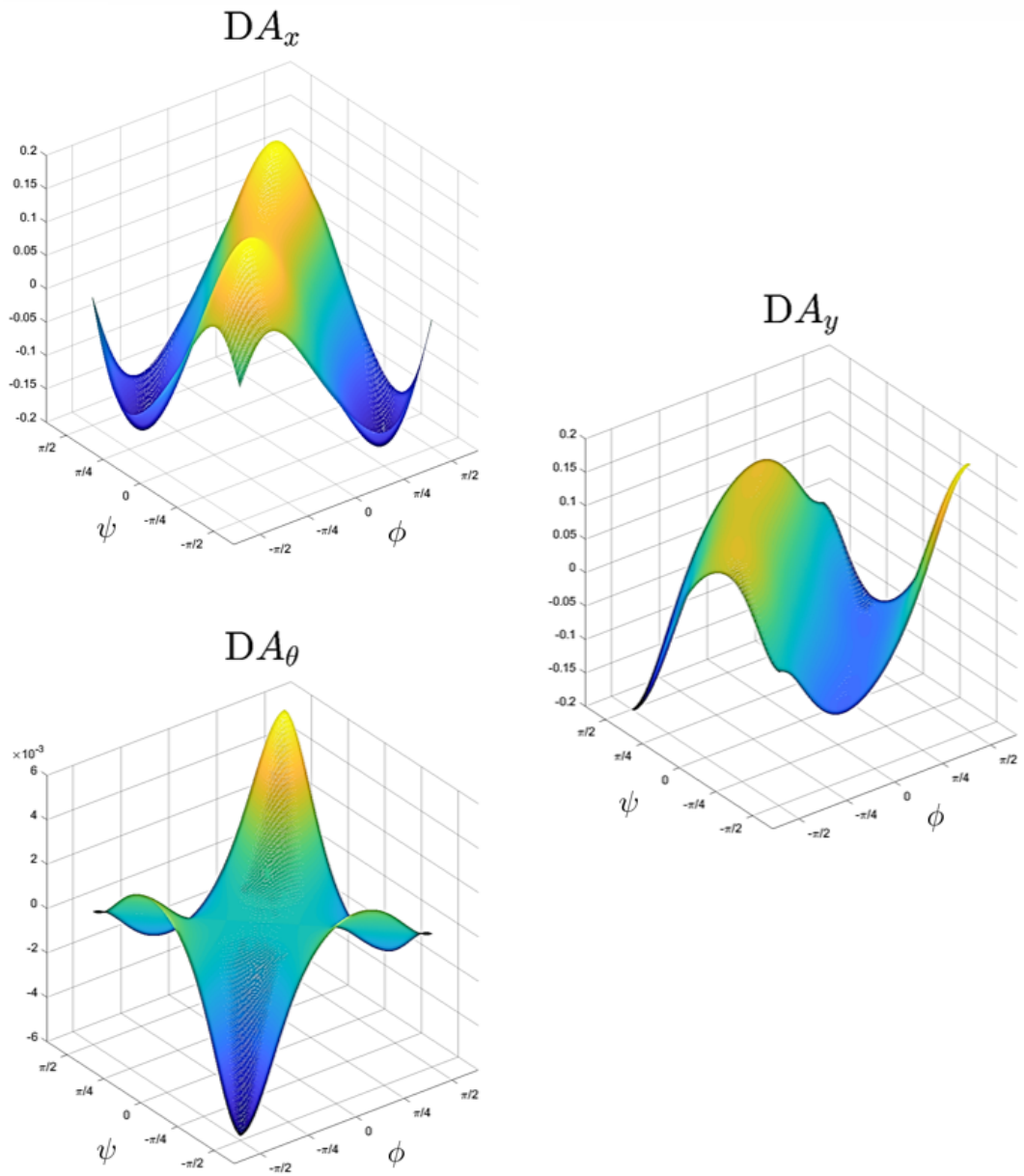

Figure 2.3: Curvature plots corresponding to the three components of $\mathfrak{se}(2)$ for the canonical three-link swimmer.

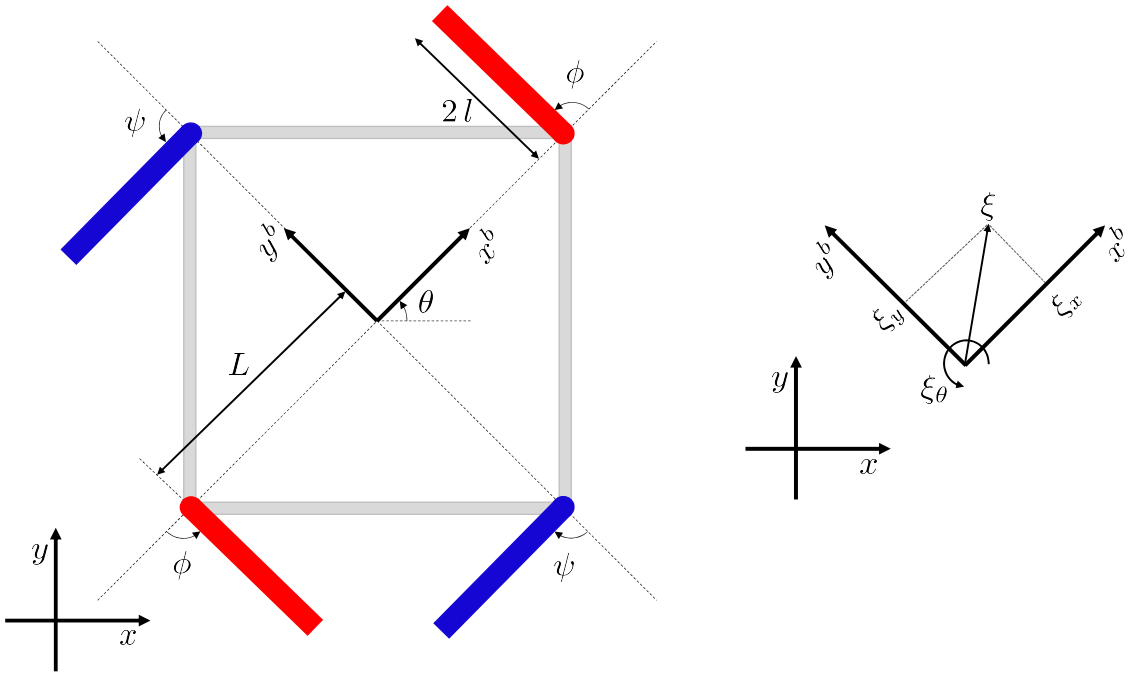

Figure 2.4: Four-paddle swimmer. *Left*: Model geometry. *Right*: Body velocity [1].

The configuration manifold for this system is

$$Q = \mathbb{T}^2 \times \mathbb{SE}(2), \tag{2.9}$$

which is the same as that for the three-link swimmer, but the local connection is different. The procedure to compute for the local connection is given in section 2.1. A difference with the previous system is that $l_i = l$ for $i = 1, \ldots, 4$.

The body velocities for the paddles are

$$\xi_1 = \begin{bmatrix} \cos(\phi)\xi_x + \sin(\phi)\xi_y + L\sin(\phi)\xi_\theta \\ -\sin(\phi)\xi_x + \cos(\phi)\xi_y + (l + L\cos(\phi))\xi_\theta + l\dot{\phi} \\ \xi_\theta + \dot{\phi} \end{bmatrix},$$

$$\xi_2 = \begin{bmatrix} -\sin(\psi)\xi_x + \cos(\psi)\xi_y + L\sin(\psi)\xi_\theta \\ -\cos(\psi)\xi_x - \sin(\psi)\xi_y + (l + L\cos(\psi))\xi_\theta + l\dot{\psi} \\ \xi_\theta + \dot{\psi} \end{bmatrix},$$

$$\xi_3 = \begin{bmatrix} -\cos(\phi)\xi_x - \sin(\phi)\xi_y + L\sin(\phi)\xi_\theta \\ \sin(\phi)\xi_x - \cos(\phi)\xi_y + (l + L\cos(\phi))\xi_\theta + l\dot{\phi} \\ \xi_\theta + \dot{\phi} \end{bmatrix},$$

$$\xi_4 = \begin{bmatrix} -\sin(\psi)\xi_x - \cos(\psi)\xi_y - L\sin(\psi)\xi_\theta \\ \cos(\psi)\xi_x - \sin(\psi)\xi_y + (l + L\cos(\psi))\xi_\theta - l\dot{\psi} \\ \xi_\theta - \dot{\psi} \end{bmatrix}.$$

We can write the generalized force vector relative to the body-fixed frame as

$$\begin{aligned}
\begin{bmatrix} F_x \\ F_y \\ M \end{bmatrix} &= \begin{bmatrix} \cos(\phi) & -\sin(\phi) & 0 \\ \sin(\phi) & \cos(\phi) & 0 \\ L\sin(\phi) & L\cos(\phi)+l & 1 \end{bmatrix} \begin{bmatrix} F_{1,x} \\ F_{1,y} \\ M_1 \end{bmatrix} \\
&+ \begin{bmatrix} -\sin(\psi) & -\cos(\psi) & 0 \\ \cos(\psi) & -\sin(\psi) & 0 \\ L\sin(\psi) & L\cos(\psi)+l & 1 \end{bmatrix} \begin{bmatrix} F_{2,x} \\ F_{2,y} \\ M_2 \end{bmatrix} \\
&+ \begin{bmatrix} -\cos(\phi) & \sin(\phi) & 0 \\ -\sin(\phi) & -\cos(\phi) & 0 \\ L\sin(\phi) & L\cos(\phi)+l & 1 \end{bmatrix} \begin{bmatrix} F_{3,x} \\ F_{3,y} \\ M_3 \end{bmatrix} \\
&+ \begin{bmatrix} -\sin(\psi) & \cos(\psi) & 0 \\ -\cos(\psi) & -\sin(\phi) & 0 \\ -L\sin(\psi) & L\cos(\psi)+l & 1 \end{bmatrix} \begin{bmatrix} F_{4,x} \\ F_{4,y} \\ M_4 \end{bmatrix}.
\end{aligned}$$

Writing this equation in the form of Equation (2.4) and equating the generalized force to zero, we obtain an equation that looks like the *kinematic reconstruction equation* (2.6) and thus acquire the local connection $A(s)$ for this system. Figure 2.5 shows the local curvature for this system as function of ϕ and ψ.

We estimate the system's net displacement and rotation over time by the equation

$$\dot{g} = -g\mathcal{A}(s, \dot{s}), \tag{2.10}$$

where g is an element of the matrix Lie Group G and can be identified as a matrix

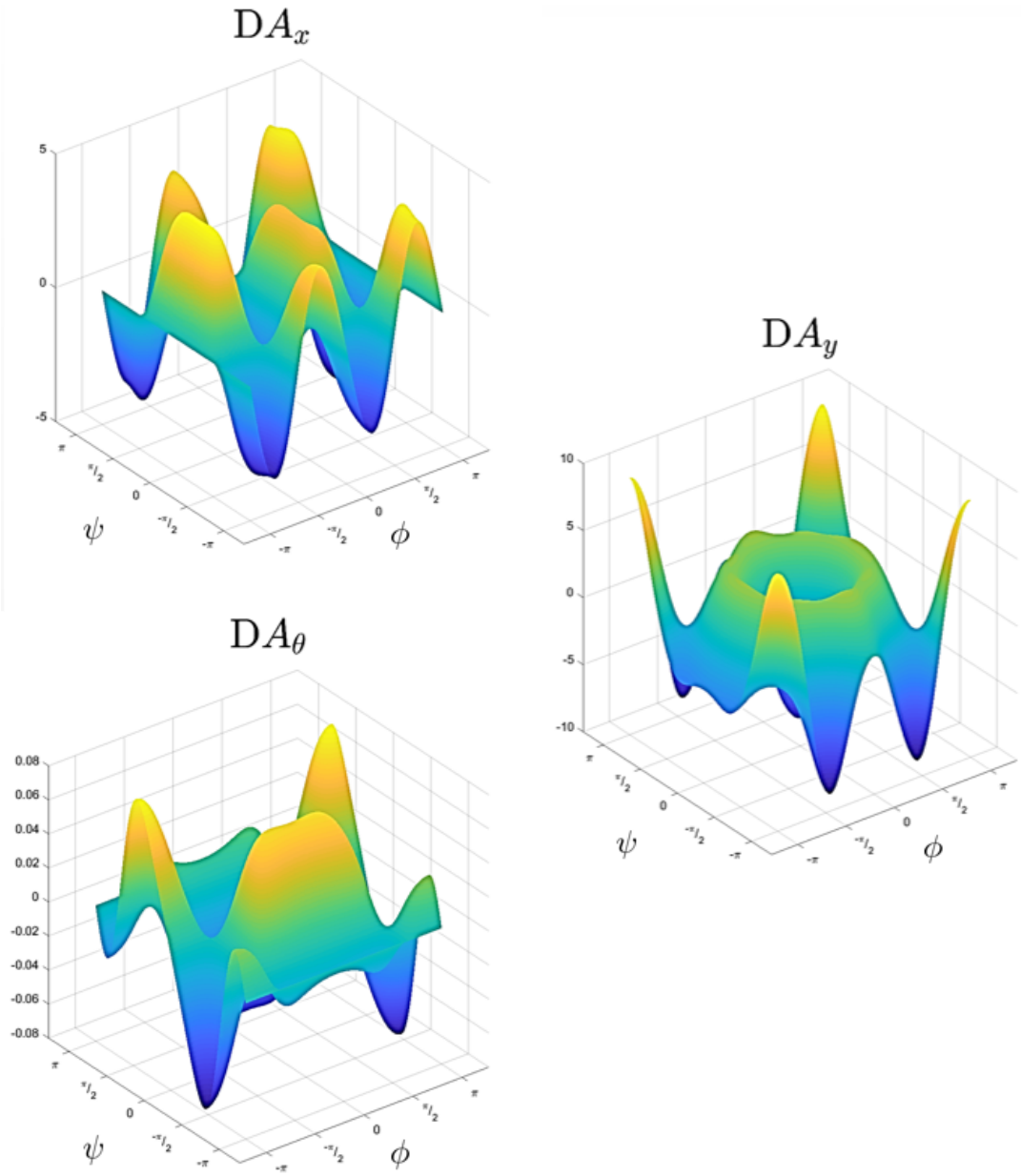

Figure 2.5: Curvature plots corresponding to the three components of $\mathfrak{se}(2)$ for the four-paddle swimmer.

of the form

$$g = \begin{bmatrix} cos(\theta) & -sin(\theta) & x \\ sin(\theta) & cos(\theta) & y \\ 0 & 0 & 1 \end{bmatrix} \in \mathbb{SE}(2)$$

and $A(s, \dot{s})$ represents the natural pairing of $\dot{s}$, thought of as a tangent vector on the shape manifold, with the local connection $A(s)$ on this manifold. The matrix multiplication of the matrices, g and $A(s, \dot{s})$, is called the left action of g on $A(s, \dot{s})$ and this action preserves the fibers in G[1].

The essential physical feature of this relationship is that $\dot{g}$ is linearly dependent on the time derivative of the body shapes $\dot{s}$. Using this relationship, we obtain the first order differential equations of motion for the system which can be numerically solved to obtain the net displacement and/or orientation.

The right panel of Figure 2.6 shows the trajectory taken by the system when subjected to cyclic changes in shape, $\phi = \frac{\pi}{4}cos(t)$ and $\phi = \frac{\pi}{4}sin(t)$. This cyclic shape change shown in the right panel of Figure 2.6 encloses circular area in the shape manifold and due to the counter-clockwise motion, results in positive displacement for negative curvature enclosed in $\mathrm{D}A_y$. The right panels of Figures 2.7 and 2.8 show the optimized loop placement for discernible net motion in x and θ respectively. Note that consequently there is some motion in y and θ as a result of some net curvature enclosed in DA_y and DA_θ.

2.3 Experimental setup and procedure

The Purcell three-link system and the four-paddle system for low Reynolds flow have similar construction with slight changes. Both systems are based on a reconfigurable platform comprising a square frame with four Pololu micro gear motors with encoders. On each motor, a paddle or link is attached to its shaft, depending on the desired configuration. The paddles were 3D printed using a PLA filament. For the

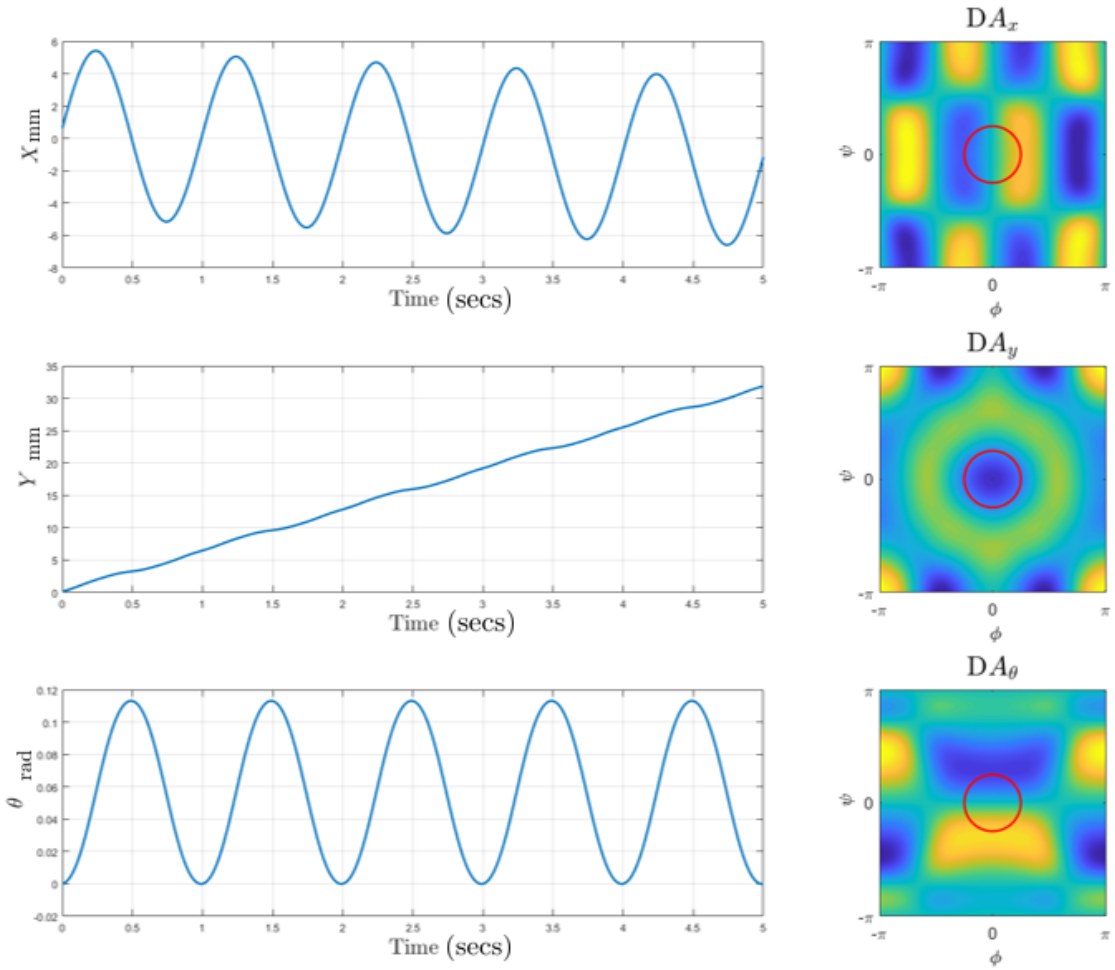

Figure 2.6: *Left*: Trajectories in the $\mathbb{SE}(2)$ coordinates *Right*: Cyclic loop placement on the curvature contours for discernible net motion in y; given $\phi = \frac{\pi}{4}cos(t)$ and $\psi = \frac{\pi}{4}sin(t)$.

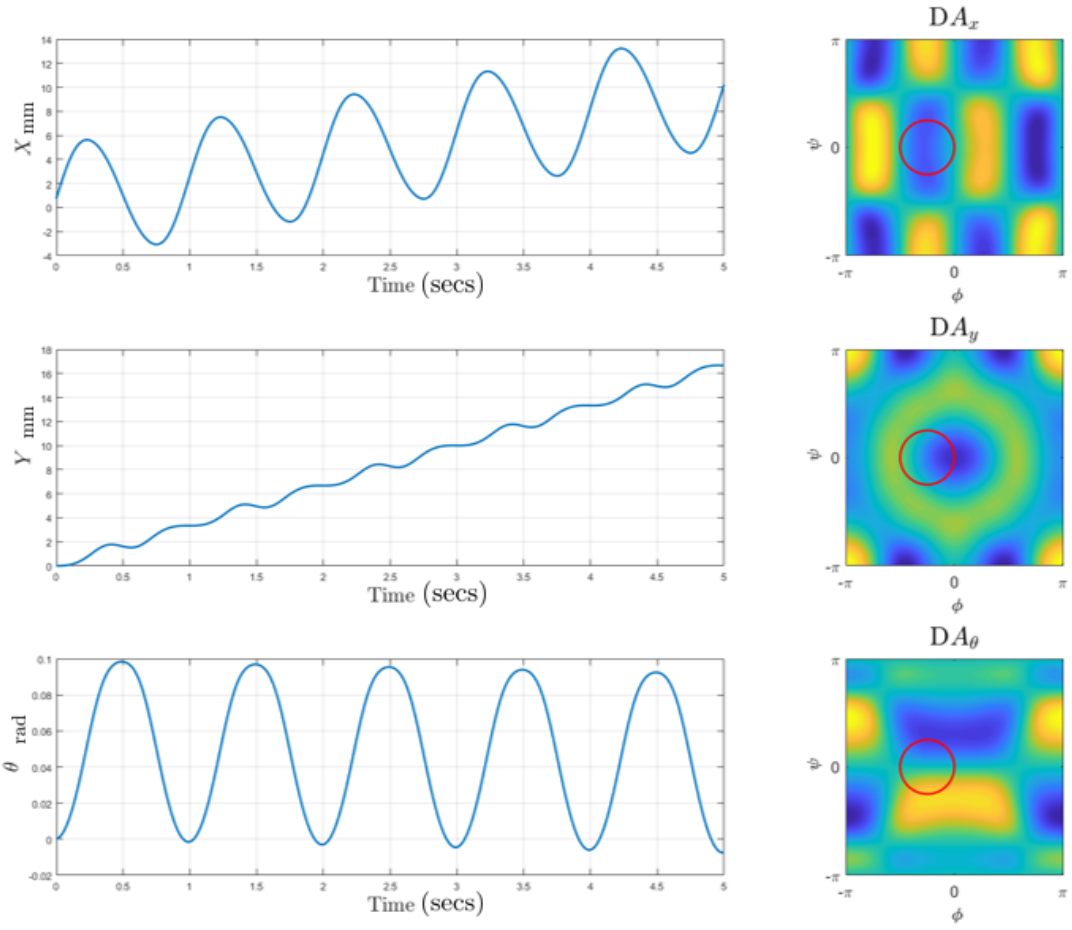

Figure 2.7: *Left*: Trajectories in the $\mathbb{SE}(2)$ coordinates *Right*: Cyclic loop placement on the curvature contours for discernible net motion in x; given $\phi = \frac{\pi}{4}cos(t) - \frac{\pi}{4}$ and $\psi = \frac{\pi}{4}sin(t)$.

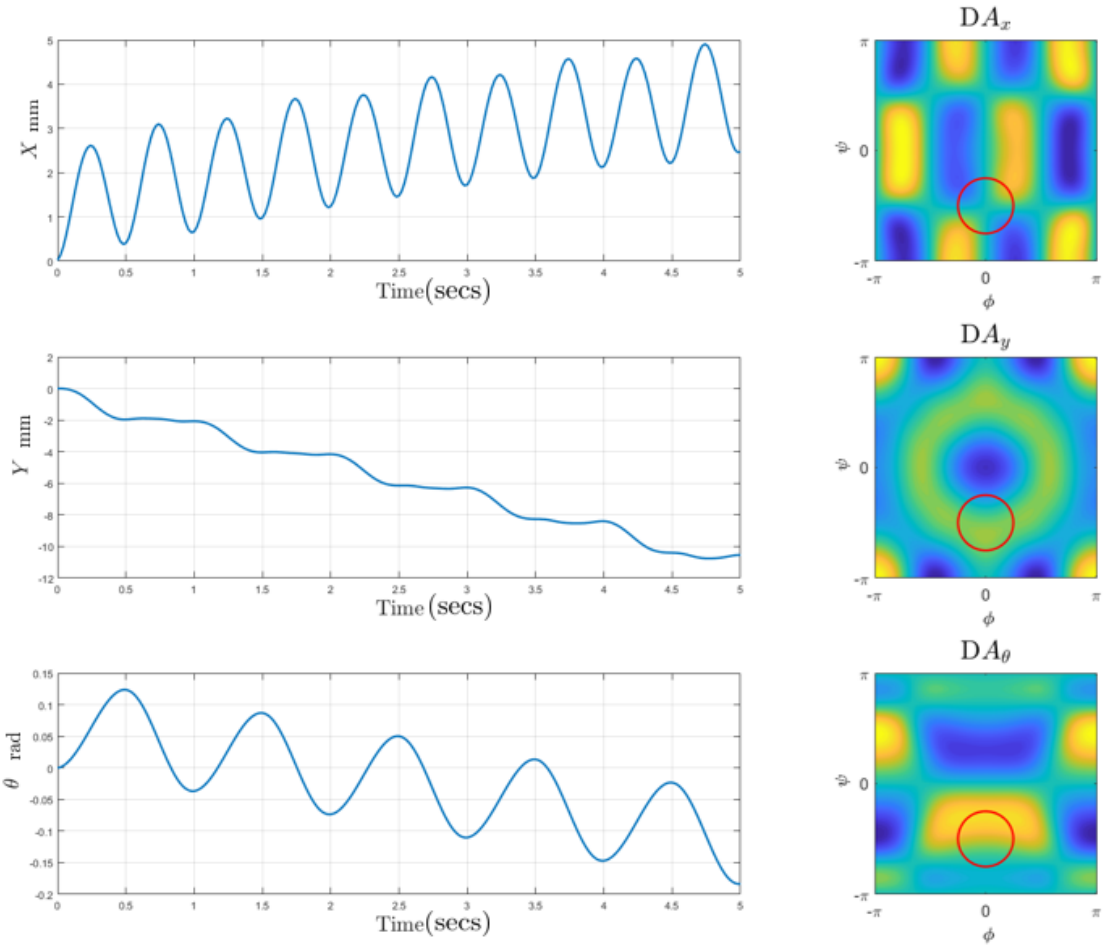

Figure 2.8: *Left*: Trajectories in the $\mathbb{SE}(2)$ coordinates *Right*: Cyclic loop placement on the curvature contours for discernible net motion in θ; given $\phi = \frac{\pi}{4}cos(t)$ and $\psi = \frac{\pi}{4}sin(t) - \frac{\pi}{2}$.

three-link swimmer, an extra passive link is added along the diagonal of the frame to act as the middle link and the other diagonal links are detached. The square frame is suspended from a horizontal beam of balsa wood with supports on the ends. Each support consists of a pink styrofoam tower shown in Figure 2.9.

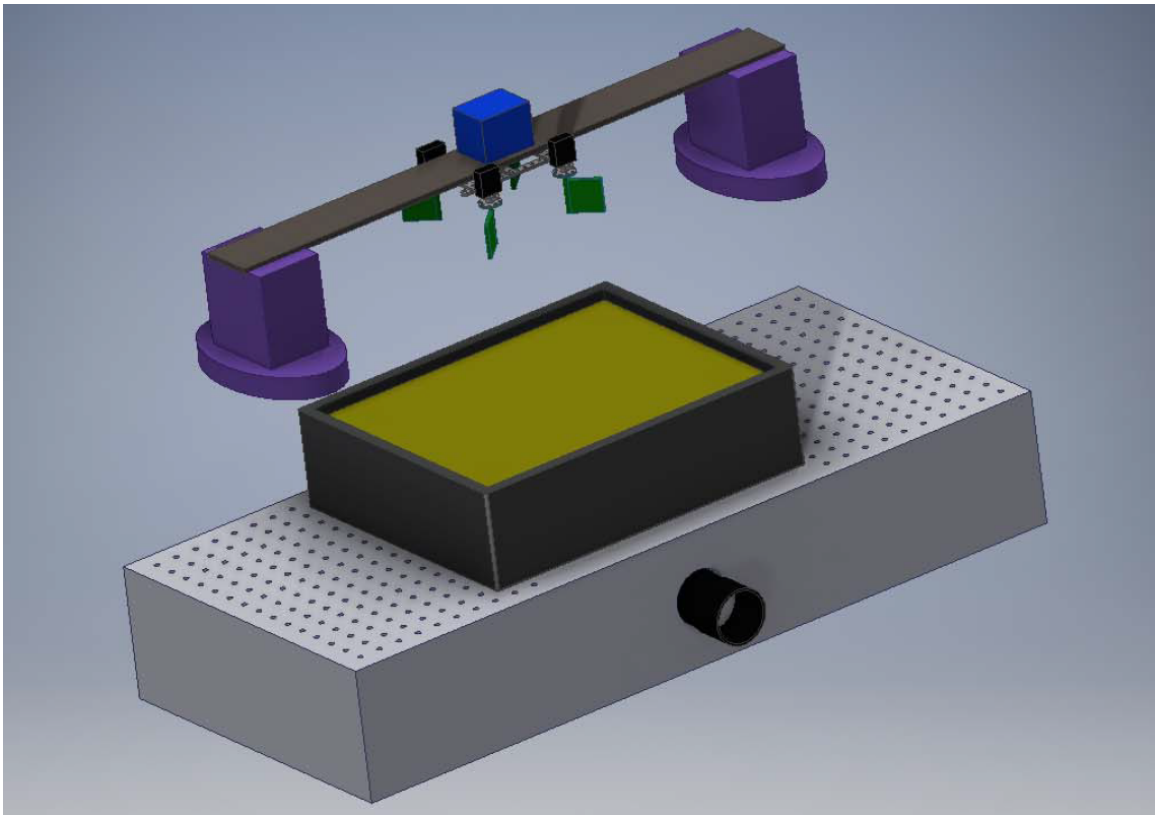

Figure 2.9: Swimmer and test bed schematic.

Mounted on the beam is an Arduino Mega microcontroller. The controller is equipped with an XBee for serial wireless communication with a PC. The electronics are powered by an on-board 6V 2200mAh NiMH battery pack which rests below the Arduino board. A PID control algorithm is employed to track and control the position of the micro gear motor shafts which is in turn connected to the paddles using aluminum hubs[1].

The swimmer is deployed in a bath of light corn syrup which has a viscosity rating of 2000 cSt, depicted in yellow in Figure 2.9. The styrofoam supports rests atop a setup

that is designed to behave like an air hockey like table. The interior of the air table is pressurized using an air blower. The surface of the air table has small orifices that allow the pressurized air to escape causing the styrofoam rafts to hover. The bottom layer of the styrofoam towers have greater surface area to provide greater amount of levitation. This helps the swimmer to avoid any friction between the setup and the air table and ensures that the interaction is only between fluid and the paddles as seen in Figure 2.10.

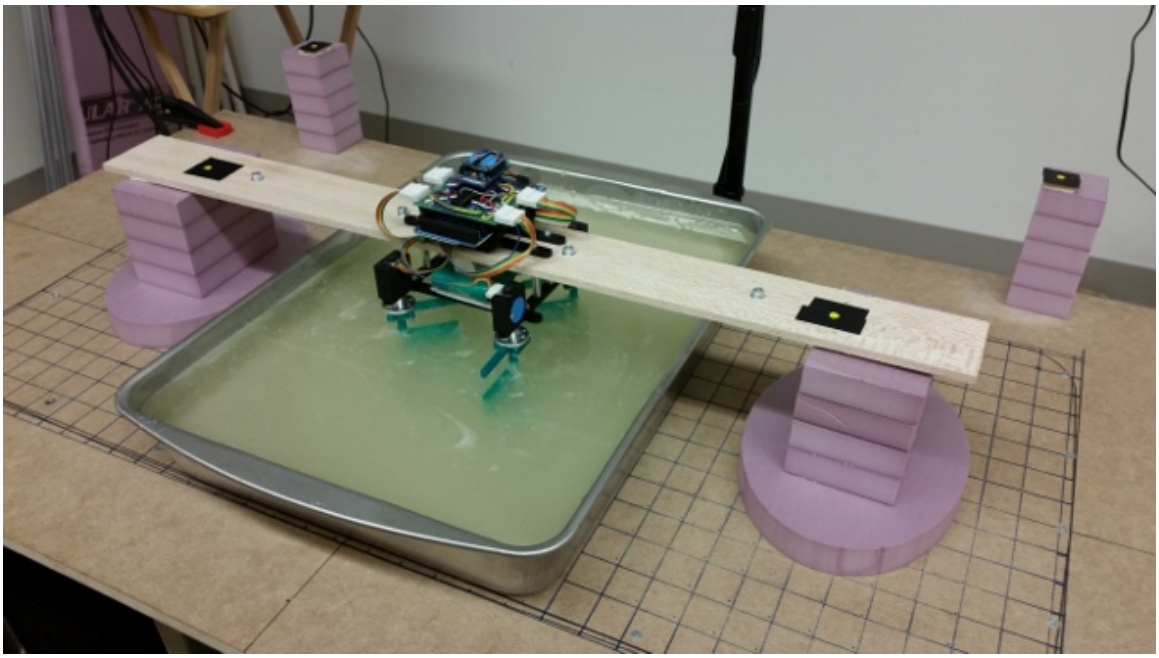

Figure 2.10: Four-paddle swimmer in fluid atop air table.

A Pi camera with a Raspberry Pi 2.0 is mounted directly above the test apparatus. Four stationary markers are positioned at the edges of the air table on seperate styrofoam towers. These are treated as the fixed reference markers for the motion tracking analysis. Two markers are placed on the wooden slat that act as the trackables. We use MATLAB's image processing toolbox to obtain the coordinates of the trackables by applying a projective transformation on the image frames with the aid of the reference markers.

Figure 2.11 depicts the physical version of the swimmers. We select a family of

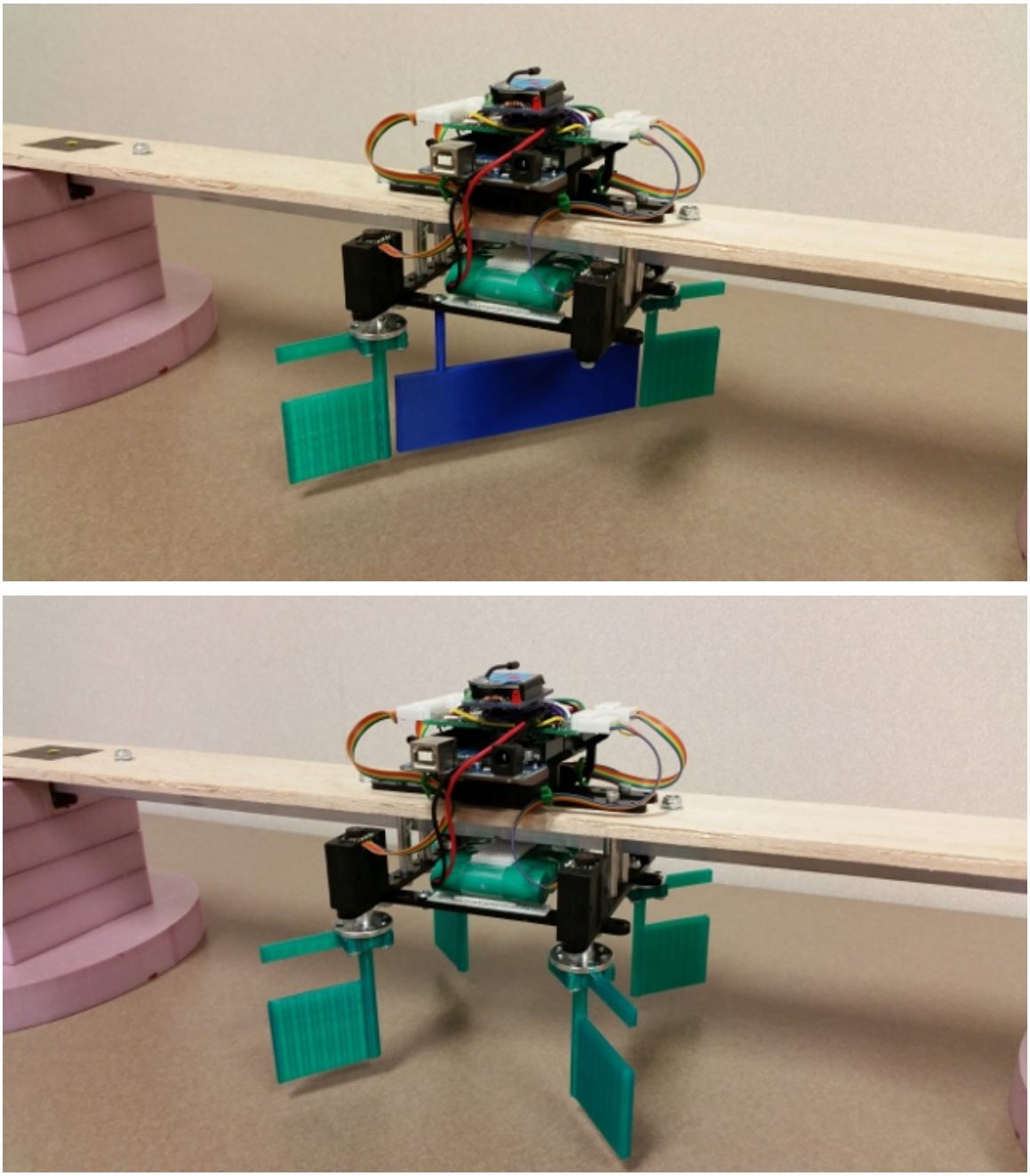

Figure 2.11: Experimental three-link swimmer and four-paddle swimmer.

square trajectories that prescribe motion to the robotic setup and tile the manifold of shapes changes. Each trajectory is centered around a shape corresponding to a different point (ϕ, ψ) in the shape manifold. We discretize the shape manifold in steps of $\pi/8$ radians and limit the shape inputs to a maximum sweep of $\pi/4$ radians during

each run. Each tile covers an area equivalent to one-fourth of the shape manifold. Overlapping of tiles helps in approximating the surface of the holonomy over the shape manifold. For the three-link swimmer, the search grid ranges from $-\pi/2$ to $\pi/2$ radians because of physical considerations in the placement of the paddles. For the four-paddle swimmer, the search grid ranges from $-\pi$ to π radians[1].

2.4 Results and discussions

The experimental local curvature is depicted in the right-hand columns of Figures 2.12 and 2.13. The shape space is discretized as a grid with a resolution of $\pi/8$ radians. Associated with each grid point is the geometric phase that corresponds with a counterclockwise square trajectory $\pi/2$ radians by $\pi/2$ radians in area[1].

The results for the three-link Purcell swimmer are shown on the right panels of Figure 2.12, and for the four-paddle swimmer on the right panels of Figure 2.13. In both cases, we plot the negative of the holonomy obtained after executing 1 cycle of the closed loop shape change. Since we mentioned that the holonomy is the exponential map from the negative of the integral of DA, Equation (2.7), we do the inverse operation to approximate the curvature. If the phase associated with a trajectory that encloses a larger area corresponds to fiberwise left translation by a group element h in the system's configuration bundle, then the matrix logarithm of h will provide an approximation to the product of the local curvature at the center of the trajectory and the area enclosed by the trajectory[1].

In both the three-link swimmer and the four-paddle swimmer, it can be seen Figures 2.12 and 2.13 that the basic structures from the theoretical plots are preserved in the experimental plot. The systematic sampling of the geometric phase associated with relatively large square trajectories in this way is sufficient to reproduce many qualitative features of the local curvatures for both swimmers. In the absence of analytical models, the right-hand columns of these figures could faithfully serve as surrogates for the left-hand columns for the purpose of selecting gaits that enclose

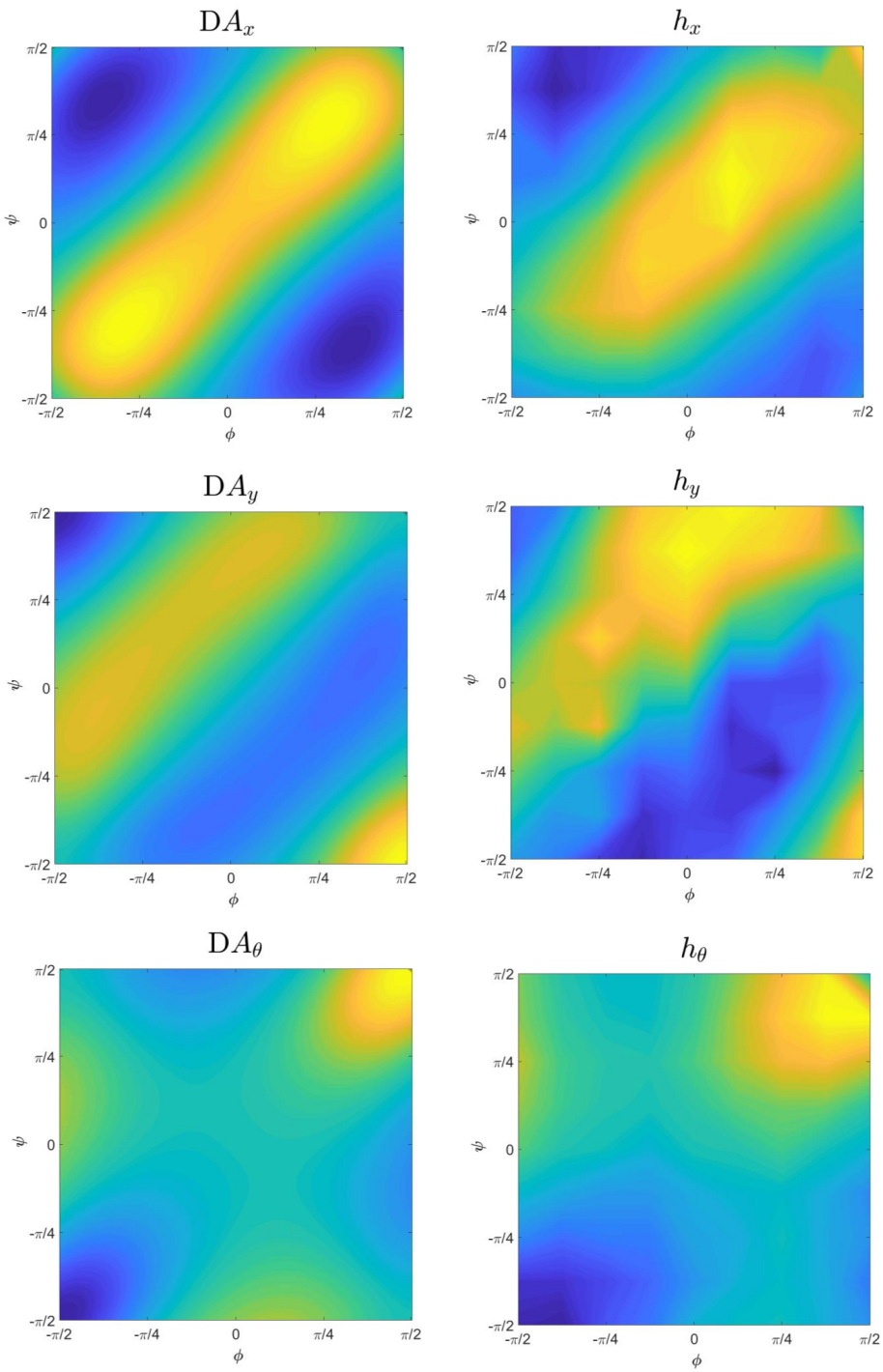

Figure 2.12: Three-link swimmer plots. *Left*: Theoretical curvature plots corresponding to the three components of $\mathfrak{se}(2)$. *Right*: Components of geometric phase (or *holonomy*) h obtained after performing closed-loop trajectories in the shape manifold, multiplied by -1 for easy comparison with the curvature plots.

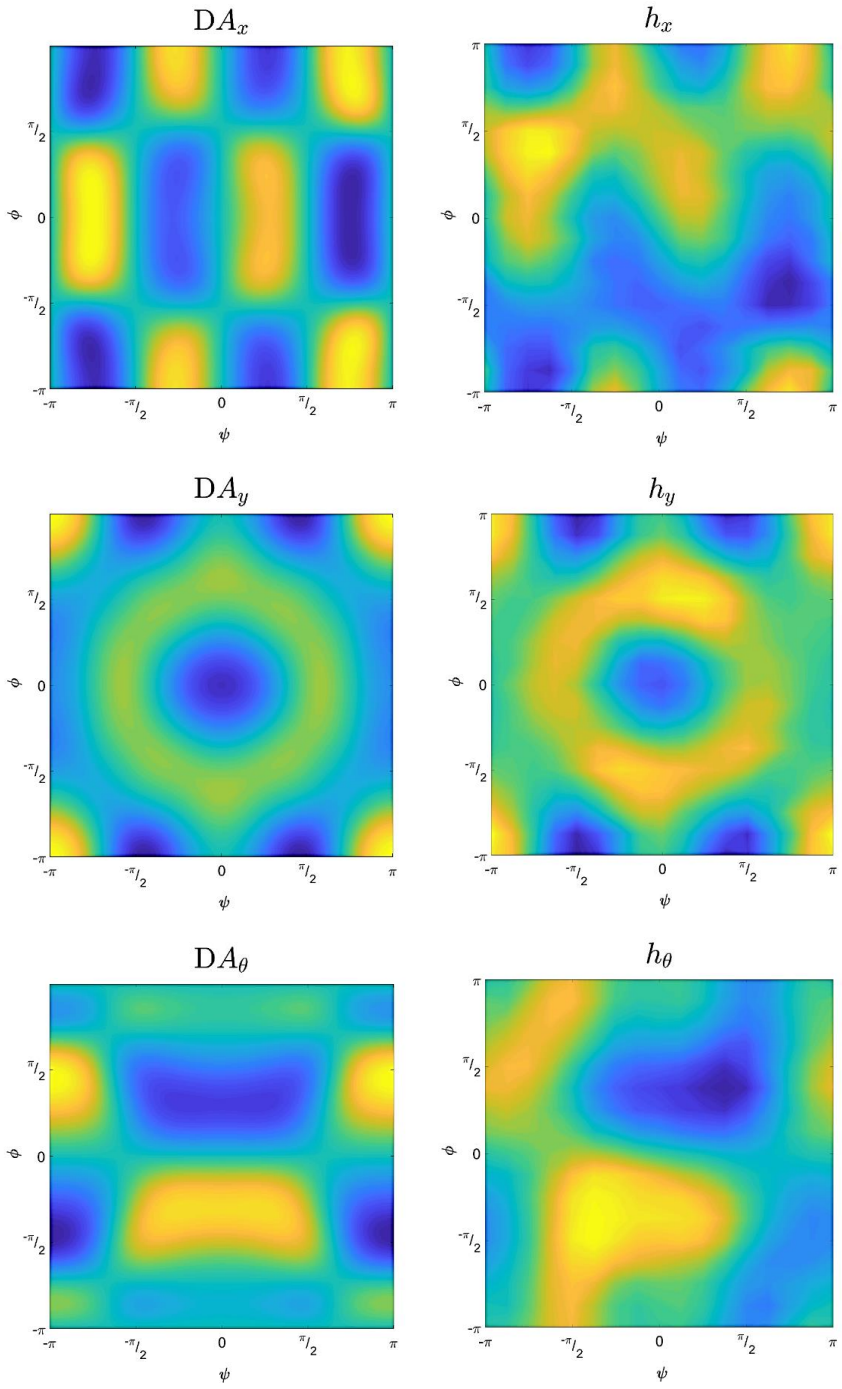

Figure 2.13: Four-paddle swimmer plots. *Left*: Theoretical curvature plots corresponding to the three components of $\mathfrak{se}(2)$. *Right*: Components of geometric phase (or *holonomy*) h obtained after performing closed-loop trajectories in the shape manifold, multiplied by -1 for easy comparison with the curvature plots.

desired combinations of positive and negative curvature[1].

CHAPTER 3: REINFORCEMENT LEARNING

Motion-planning and navigation of robots in the absence of a dynamic model can be explored using techniques in reinforcement learning (RL). RL is a reward based machine learning technique applied to problems in automatic control, artificial intelligence, et cetera. A simple schematic of RL is shown in Figure 3.1, the agent gets input from the environment in the form of states and performs actions to maximize the returns in the form of rewards accumulated over a sequence of consecutive runs. In this thesis, we apply this technique to the aforementioned systems and learn an optimal sequence of actions/shape changes in order achieve a desired goal over an extended period of time.

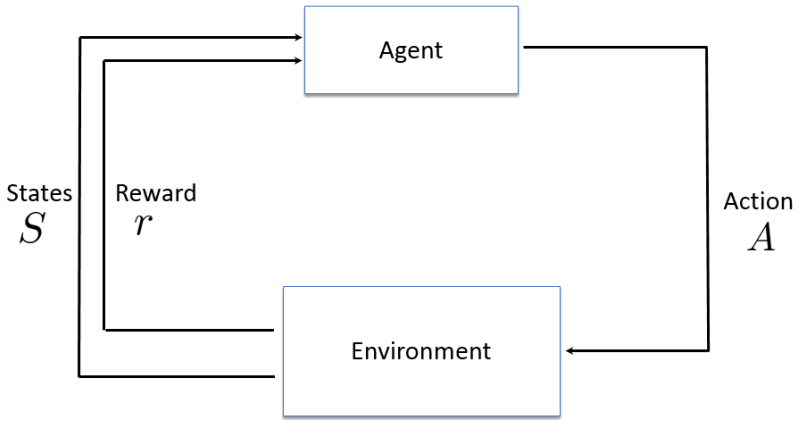

Figure 3.1: Reinforcement Learning

RL problems are formalized with MDPs or Markov Decision Processes. *"Markov decision processes (MDPs) provide a mathematical framework for modeling decision making in situations where outcomes are partly random and partly under the control of a decision maker"* [22]. Every entity of the system that changes with an action a applied to it is called a state s. A state-action transition is said to satisfy the Markov

property if the current state action pair is sufficient to dictate the transition to the next state [23].

A state s_k at step k transitions to a new state s_{k+1} under some action a_k according to the transition function $f : S \times A \to S$:

$$s_{k+1} = f(s_k, a_k), \tag{3.1}$$

and associated with each transition is a scalar reward r_{k+1} according to the reward function $\rho : S \times A \to \mathbb{R}$:

$$r_{k+1} = \rho(s_k, a_k). \tag{3.2}$$

The controller chooses actions according to its policy $h : S \to A$, given by

$$a_k = h(s_k). \tag{3.3}$$

To seek a way to characterize the policy h, we define state-action function called the Q-function according to $Q^h : S \times A \to \mathbb{R}$ of a policy h

$$Q^h(s, a) = \rho(s, a) + \gamma Q^h(f(s, a), h(f(s, a)), \tag{3.4}$$

where $\gamma \in (0, 1]$ is the discount factor. Equation 3.4 is called the *Bellman equation*[23].

The Q-function that is defined to be the optimal Q-function at any policy is given by:

$$Q^*(s, a) = \max_h Q^h(s, a), \tag{3.5}$$

and any policy h^* defines the action for each state with the largest Q-value satisfies:

$$h^*(s) \in \arg\max_a Q^*(s,a). \tag{3.6}$$

A policy acts *greedy* in Q if it satisfies

$$h(s) \in \arg\max_a Q(s,a). \tag{3.7}$$

The optimal policy can be computed by finding Q^* and then extracting h^*. This policy is said to be *greedy* in Q^*.

The *Bellman optimality equation* can be defined as

$$Q^*(s,a) = \rho(s,a) + \gamma \max_{a'} Q^*(f(s,a),a'), \tag{3.8}$$

where $a' \in A$ is the action that maximizes Q^* at the transitioned state[23].

3.1 Q-learning

We describe the implementation of an RL technique categorized as *Q-learning*. Q-learning is a classical RL technique applied to discrete systems and is classified as a *temporal difference* method [23]. It can be implemented off-line as well as on-line depending on the availability of the system dynamics. It is an iterative learning technique that evaluates a policy after each episode[1]. The Q-function is initialized as a tabular matrix with some arbitrary Q_0 values. Each cell within the Q-function corresponds to a state-action pair and updated at each time-step k based on the state transition and reward according to:

$$Q_{k+1}(s,a) = Q_k(s,a) + \alpha_k(r_{k+1} + \gamma \max_{a'} Q_k(s_{k+1},a') - Q_k(s_k,a_k)), \tag{3.9}$$

[1]An episode is defined as a pre-defined number of actions that the system can execute to achieve the desired goal and is also known as a trial.

where $\alpha_k \in (0, 1]$ is the learning rate. The term multiplied by the learning rate is called the temporal difference. The following conditions need to be met in order for Q-learning to converge to h^*:

1. states and action spaces need to be discrete and finite,
2. as k approaches infinity, the value of α should asymptotically approach 0 to stop the learning process and attain convergence and
3. all state-action pairs need to be visited adequately.

An α-decay constant is implemented to ensure that α approaches 0 as k increases. To improve exploration of the state-action spaces, we apply an ϵ-greedy policy search that selects actions according to:

$$a = \begin{cases} a \in \arg\max_{a'} \mathrm{Q}(s, a), & \text{with probablity 1-}\epsilon \\ \text{a random action in } A, & \text{with probability } \epsilon \end{cases}$$

But the learning will never converge to h^* if the algorithm takes some random action ϵ amount of times for all time. This trade off is settled by having an ϵ-decay constant analogous to the α-decay constant[23].

The algorithm is implemented for an infinitely large k and the convergence depends upon the tuning of ϵ, α and their decay constants respectively. A pseudo-code for Q-learning is shown in Algorithm 1

Researchers have extensively applied Q-learning on problems like the navigation of a robot through a simple maze, playing backgammon [24], et cetera. To validate this model and to present as an example problem, we apply this algorithm to control a pendulum at its upright position. We define our states as the angular displacement θ and the angular velocity $\dot{\theta}$, and our action is the control torque T needed to swing the pendulum upright. Our reward function maximizes the return as the iterative state $\rightarrow$ goal state. We treat this problem in its discrete form and apply a fine discretization to

Algorithm 1 Off-line Q-learning algorithm

Require: Discount factor-γ, Learning rate-α, Exploration schedule-ϵ, α-decay rate, ϵ-decay rate, reward function

Initialize: $Q(s,a) \Leftarrow 0\ \forall s,a$

for N number of episodes **do**

Prescribe: initial condition s_0

for each time step k **do**

$$a_k \Leftarrow \begin{cases} a_k \in \arg\max_{a'} \mathrm{Q}(s,a'), & \text{with probablity 1-}\epsilon \\ \text{a random action in } A, & \text{with probability } \epsilon \end{cases}$$

Solve: system ODEs by applying control action a_k using Runge Kutta methods;

Measure: state s_{k+1} and corresponding reward r_{k+1}.

Compute: $Q_{k+1}(s_k,a_k) \Leftarrow Q_k(s_k,a_k) + \alpha_k(r_{k+1} + \gamma \max_{a'} Q_k(s_{k+1},a') - Q_k(s_k,a_k))$

end for

Continue until: convergence criterion satisfied

end for

Extract Optimal Policy: $h^*(a) \in \max_a Q(s,a)\ \forall s,a$

θ and $\dot{\theta}$ and specify a range for T. We let the algorithm perform the computation until our convergence criterion is satisfied. The convergence criterion for our case is the balancing of the pendulum in its upright position. We find convergence for a finite number of initial conditions after 245 iterations. Figure 3.2 depicts the extracted policy that gives information about the necessary actions that the pendulum needs to perform to reach the goal state, given any initial conditions. Based on the policy diagram (Figure 3.2), we can identify the best possible control route to reach the goal state, given any initial condition.

3.1.1 Q-learning on the four-paddle swimmer

We now focus our attention to the implementation of the Q-learning technique to seek the maximized x-directional translation of the four-paddle swimmer with respect to a laboratory frame of reference, given a set of initial conditions. As seen in Section 2.2, the configuration manifold for the four-paddle robot is $\mathbb{T}^2 \times \mathbb{SE}(2)$. We denote all the variables associated with this configuration manifold (x, y, θ, ϕ and ψ) to be our

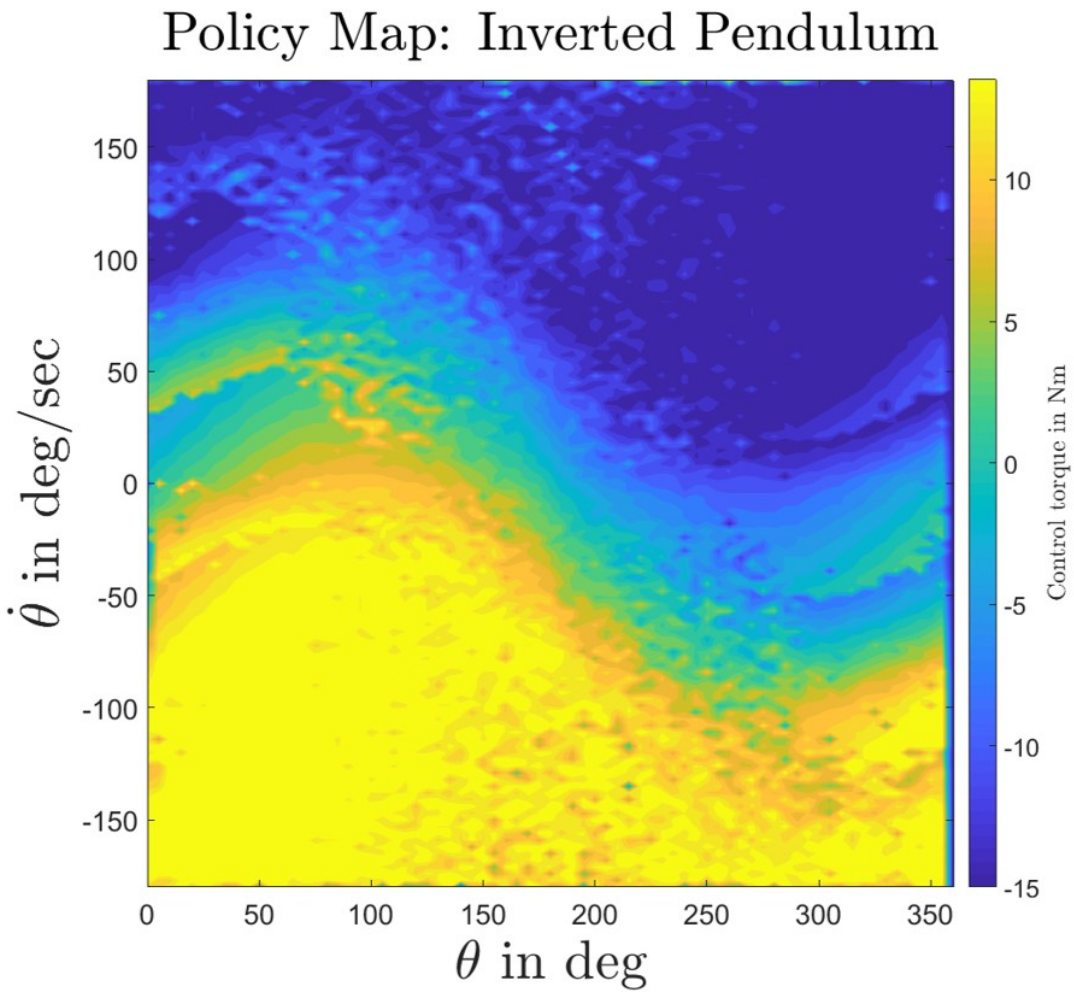

Figure 3.2: Policy map of the inverted pendulum control problem.

states, and the rate of change of joint angles $\dot{\phi}$ and $\dot{\psi}$ as our actions. We discretize ϕ and ψ in steps of $\frac{\pi}{34}$ radians ranging from $-\pi$ to π and limit the rate of change of joint angles within $[-2\pi, 2\pi]$ radians/sec discretized in steps of $\frac{\pi}{50}$ radians/sec. We define the Q-function as four-dimensional matrix and initialize it with a scalar Q-value for each quadruple combination of ϕ, ψ, $\dot{\phi}$ and $\dot{\psi}$ and disregard the external fiber variables(x, y and θ) as the translation mechanism for this system is independent of these variables. These Q-values are rewarded within each episode by the reward function which is a scaled multiple of the longitudinal distance x found by solving for the dynamics of the system when the internal states are initialized to ϕ and ψ, and $\dot{\phi}$ and $\dot{\psi}$ are the inputs to the system. Due to the high-dimensionality nature of this

problem, the amount of iterations needed to reach convergence is enormously larger. We simulate the system by varying the initial orientation of the system and perform an episode over a fixed number of control actions. In order to explore a large number of control sequences, we apply the ϵ-greedy decay constant for 70% of the simulations, after which the algorithm is made to act greedy only. To achieve convergence, we run the simulation for 5 million episodes with each episode executing a control action at every 0.25 secs for 20 time-steps and leaving the initial condition unchanged. Each time-step corresponds to a control action.

The left-hand side image on Figure 3.3 displays the trajectory of the system. The output of the algorithm shows that the first few control actions align the orientation and internal shape of the 4-paddle swimmer in order to perform optimal translation in the future. Due to the presence of non-holonomic constraints in the system, the algorithm sacrifices on short-term rewards and focuses on the far-sighted goal of moving as much as possible in the x-direction throughout the episode. It is seen that this is clearly achieved by executing cyclic actuation. The right-hand side image on Figure 3.3 shows that these cyclic actuations execute closed loops on the manifold of shapes and enclose curvature according to the geometric theory. Each point in the right hand image of Figure 3.3 constitutes a pair of piecewise constant control action ($\dot{\phi}$ and $\dot{\psi}$) executed on the system at each time-step.

To verify that our analysis holds true for different conditions, we vary the initial orientation of the system without changing the objective which is to maximize the x-translation. This is depicted in Figure 3.5 and Figure 3.4. The plots indicate that the best way for the system to translate is by actuating repetitive control sequences which form closed loops on the manifold of shapes and enclose curvature as shown before.

Over shorter time scales, the optimal locomotion of the system adapts itself with respect to the initial condition and takes long lunges so as to translate in the x-

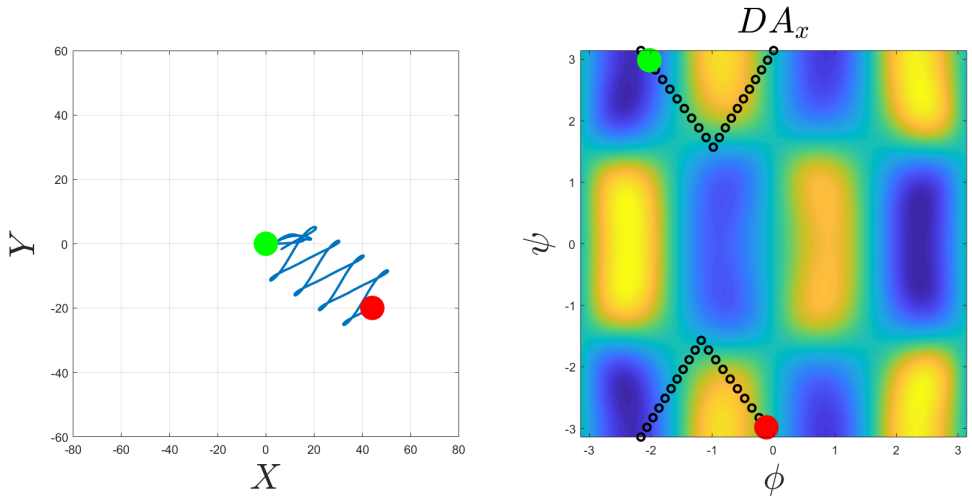

Figure 3.3: Motion with respect to the lab frame; θ was initialized to 0 radians. *Left*: Trajectory of the system on the lab frame. *Right*: Cyclic loop placement over the local curvature of the x component of $\mathfrak{se}(2)$. Green blob indicates start and red blob indicates the end.

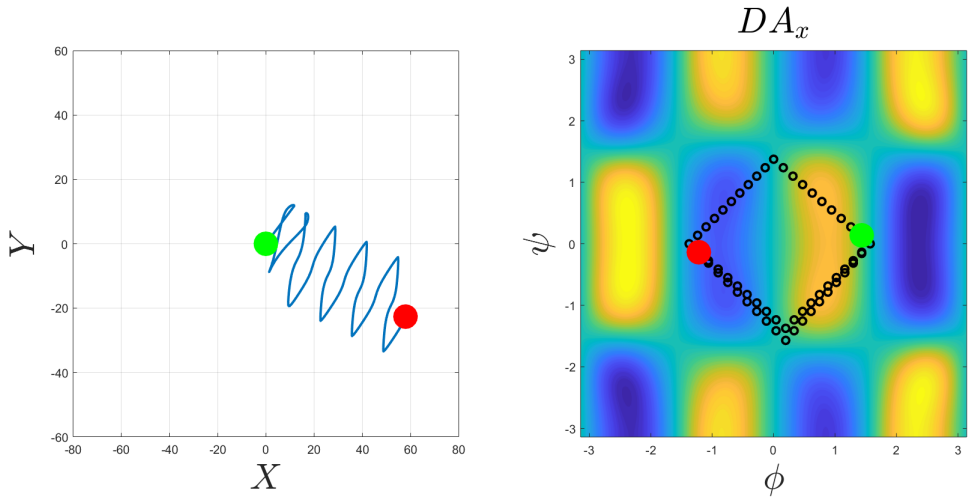

Figure 3.4: Motion with respect to the lab frame; θ was initialized to $\pi/4$ radians. *Left*: Trajectory of the system on the lab frame. *Right*: Cyclic loop placement over the local curvature of the x component of $\mathfrak{se}(2)$. Green blob indicates start and red blob indicates the end.

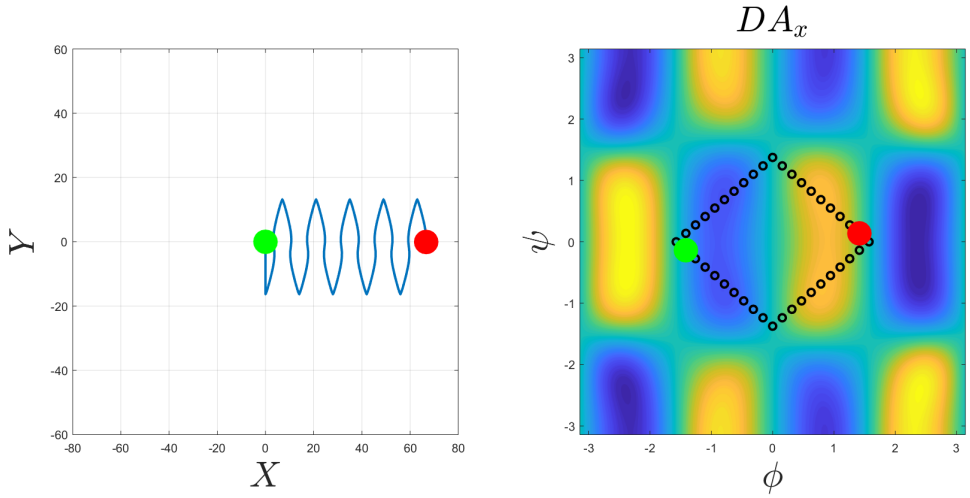

Figure 3.5: Motion with respect to the lab frame; θ was initialized to $\pi/2$ radians. *Left*: Trajectory of the system on the lab frame. *Right*: Cyclic loop placement over the local curvature of the x component of $\mathfrak{se}(2)$. Green blob indicates start and red blob indicates the end.

direction as shown in Figure 3.6, Figure 3.7 and Figure 3.8. As the system approaches a state where it can no longer translate in the intended direction, the algorithm identifies that the best control action is for the system to stay at rest as seen Figures 3.6, 3.8 and 3.7.

Until now, we have only defined the translation of the system only with reference to an arbitrary laboratory frame. Figure 3.9 shows the translation of the system when the objective of the system is altered to maximize the x-translation with respect to the robot's body frame. We assume that the body fixed frame of the robot is centered at the centroid of the system geometry. It is observed that extracted policy indicates that cyclic actuation maximizes the translation in every possible move which is in agreement with the geometric theory.

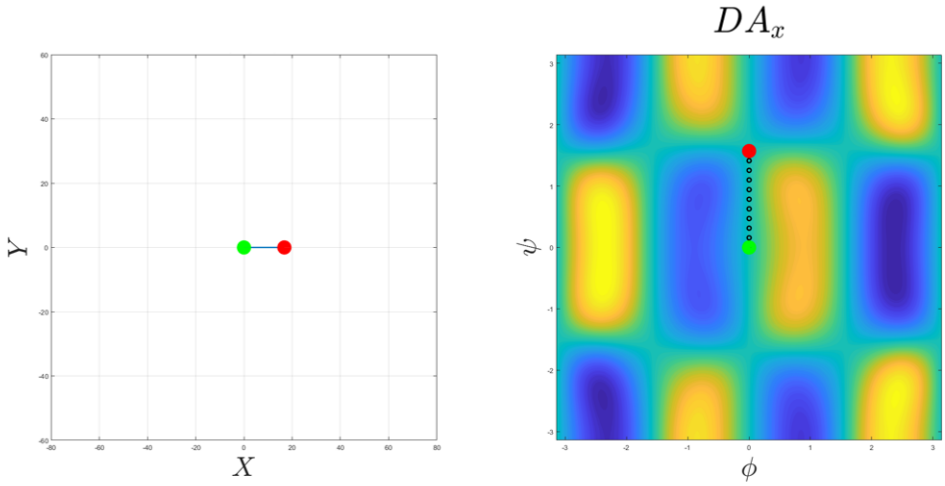

Figure 3.6: Motion with respect to the lab frame simulated over a shorter four time-step episode; θ was initialized to 0 radians. *Left*: Trajectory of the system on the lab frame. *Right*: Cyclic loop placement over the local curvature of the x component of $\mathfrak{se}(2)$. Green blob indicates start and red blob indicates the end.

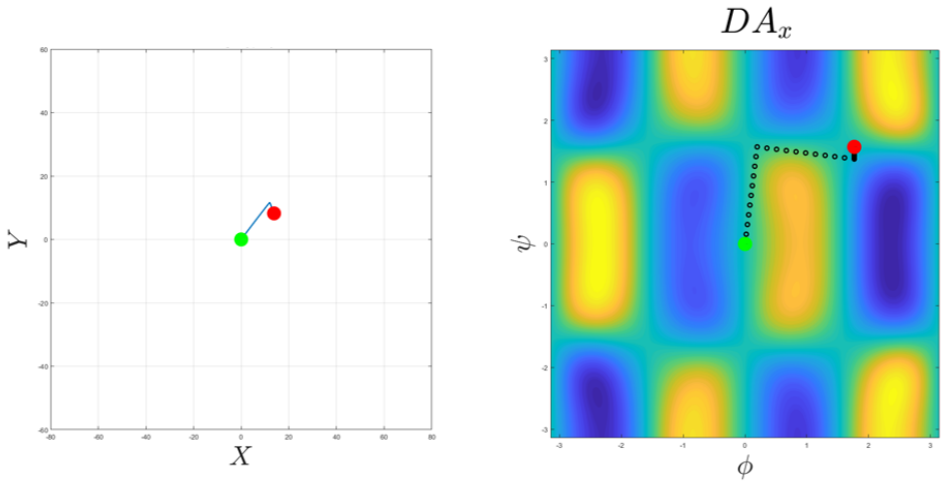

Figure 3.7: Motion with respect to the lab frame simulated over a shorter four time-step episode; θ was initialized to $pi/4$ radians. *Left*: Trajectory of the system on the lab frame. *Right*: Cyclic loop placement over the local curvature of the x component of $\mathfrak{se}(2)$. Green blob indicates start and red blob indicates the end.

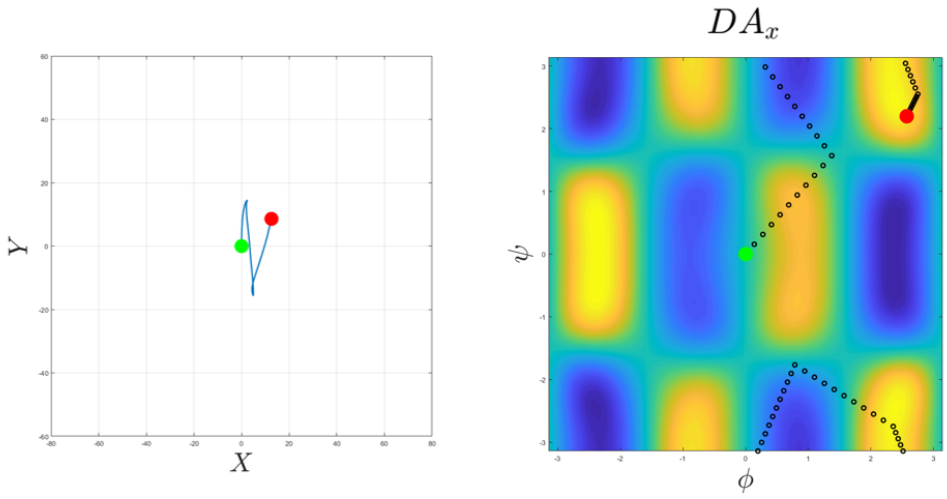

Figure 3.8: Motion with respect to the lab frame simulated over a shorter four time-step episode; θ was initialized to $pi/2$ radians. *Left*: Trajectory of the system on the lab frame. *Right*: Cyclic loop placement over the local curvature of the x component of $\mathfrak{se}(2)$. Green blob indicates start and red blob indicates the end.

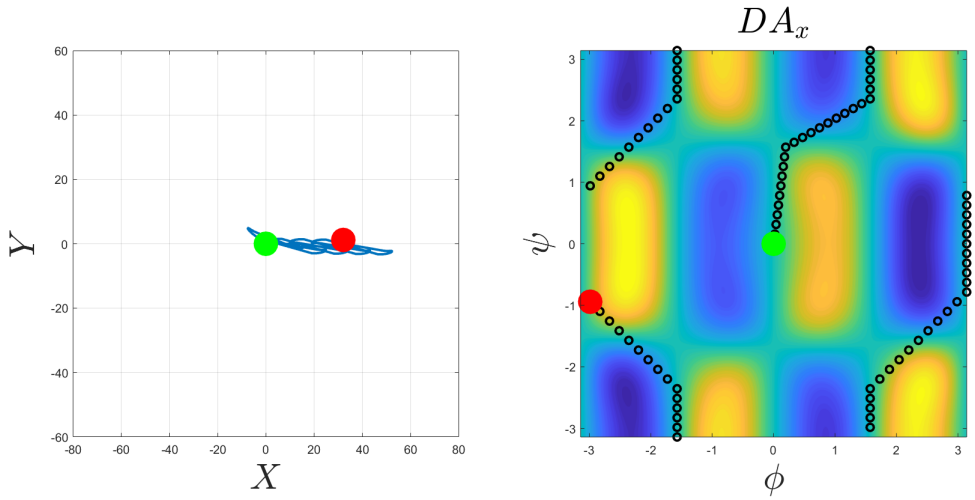

Figure 3.9: Motion with respect to the body frame; θ was initialized to 0 radians. *Left*: Trajectory of the system on the lab frame.*Right*: Cyclic loop placement over the local curvature of the x component of $\mathfrak{se}(2)$. Green blob indicates start and red blob indicates the end.

CHAPTER 4: SYSTEMS IN HIGH REYNOLDS FLOW

It is common knowledge that the pitching action of a hydrofoil is similar to the flapping of a bird or the oscillating motion of a fish's tail. The formation of non-linear vortices in the wake of the flapping hydrofoil dominate the dynamics of flow. When a group of hydrofoil like bodies are placed in closed proximity in the flow, it is believed that the vortices interact hydrodynamically and the nature of these vortex interactions is directly associated with the kinematics of oscillating bodies. These interactions may be constructive or destructive with respect to the forward propulsion of the hydrofoil and depend upon the placement of the hydrofoils and the type of actuation.

Complex fluid flow solvers take into account many of these vortex effects to simulate the dynamics of the flow, but at the cost of high computational requirements and considering many unrealistic assumptions. Researchers in this area have largely focused on experimental data for reliable assertions for multiple-body interactions in high Reynolds number flow regimes.

One of the aims of this thesis is to the quantify performance characteristics of a system with multiple hydrofoils/paddles that self-propel in water via pitching. We talk about some of these performance characteristics in this section and define some of the terms associated -

The propulsive efficiency η, also called the Froude efficiency, is defined as the ratio of useful power output to the power input to the system and is represented as

$$\eta = \frac{F_x u_\infty}{P}, \tag{4.1}$$

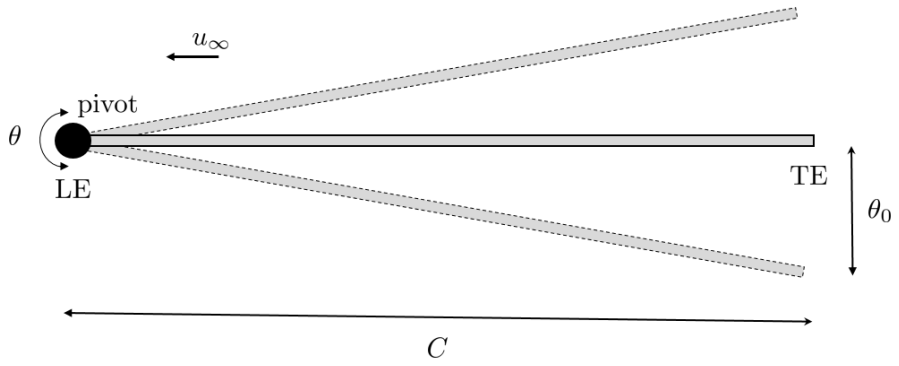

Figure 4.1: Cross-sectional view of the hydrofoil.

where F_x is the cycle averaged force, P is the cycle averaged input power to the system and u_∞ represents the swimming speed of the system. The thrust coefficient is given by

$$C_T = \frac{F_x}{\frac{1}{2}\rho u_\infty^2 sC}, \tag{4.2}$$

and the coefficient of power is given as

$$C_P = \frac{P}{\frac{1}{2}\rho u_\infty^3 sC}, \tag{4.3}$$

where s is the span of the hydrofoil and ρ is the fluid density.

Figure 4.1 depicts the a planar hydrofoil, where C is the chord length, b is its thickness and θ_0 is the amplitude of the prescribed oscillation. The pitching angle is specified by θ and the ratio of the span to chord length s/C is equal to 1. LE is the leading edge and TE is the trailing edge of the hydrofoil. The swimming speed u_∞ is analogous to free stream velocity. The pitching of the hydrofoil is about its pivot which is connected to the actuator, and the span of the hydrofoil submerges into the water.

The Reynolds number is given by the equation

$$Re = \frac{\rho u_\infty C}{\mu}, \tag{4.4}$$

where the μ is the dynamic viscosity of water (0.89 cP).

We consider two types of multi-hydrofoil configurations. The first one is the two-hydrofoil configuration depicted in Figure 4.2. The length of each hydrofoil is C and its oscillation is parameterized by θ with respect to its pivot. We oscillate the hydrofoils out-of-phase with respect to one another to avoid maneuvers due to the moment generated by thrust imbalance and to achieve maximum thrust performance [18] in the longitudinal direction. We represent the pitching angle of the second hydrofoil by a * superscript indicating out-of-phase pitching relationship. The oscillations of the hydrofoils are given by $\theta = \theta_0 sin(2\pi ft)$ and $\theta^* = \theta_0 sin(2\pi ft + \pi)$, where θ_0 is the amplitude, f is the frequency, and t is time. The lateral spacing between the two hydrofoils is scaled by multiples of paddle chord length C.

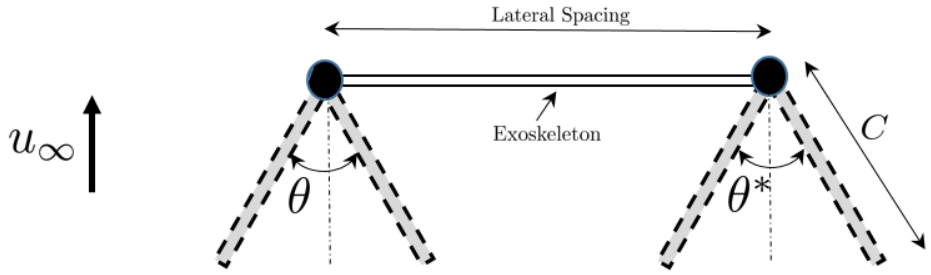

Figure 4.2: Two-hydrofoil hydrodynamic swimmer schematic.

The next system considered is a four-hydrofoil quadrilateral configuration, analogous to the novel system considered in Section 2.2, and is shown in Figure 4.3. This type of arrangement can be visualized as a robotic fish school where the spacing among hydrofoils can be varied both laterally and longitudinally and these spacings

are scaled by multiples of hydrofoil chord length C. The oscillation prescribed to the Front Row(FR) hydrofoils is the same as the sinusoidal pitching actuation of the two-hydrofoil system with oscillations θ and θ^*. The oscillation prescribed to the Back Row(BR) hydrofoils is given by $\alpha = \theta_0 sin(2\pi ft + \phi)$ and $\alpha^* = \theta_0 sin(2\pi ft + \phi + \pi)$ where ϕ is the phase difference between the FR and BR hydrofoils.

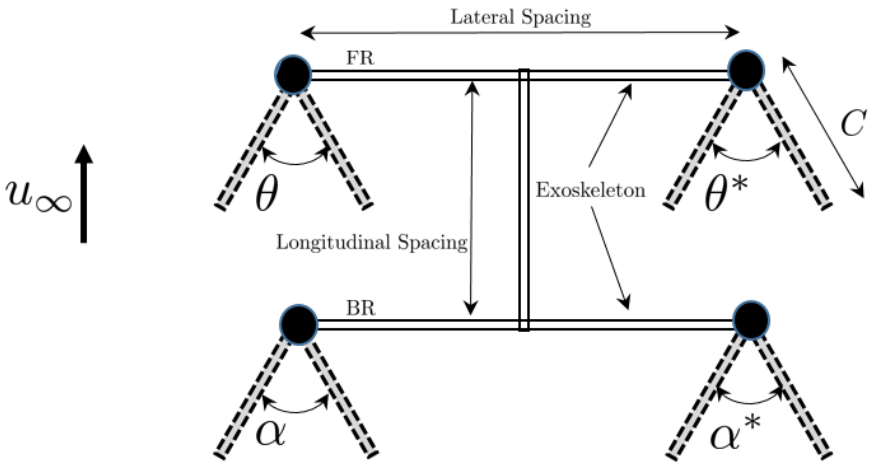

Figure 4.3: Two-hydrofoil hydrodynamic swimmer schematic. FR indicates the front row and BR is the back row.

4.1 Experimental setup and procedure

The construction of the high Reynolds number multi-hydrofoil systems are based on a reconfigurable exoskeleton. The exoskeleton comprises of 3' long balsa wood slats resting on two styrofoam supports at the ends. In addition to providing support, these styrofoam blocks make the structure buoyant. The slats are reinforced with aluminum channels on the flip side to avoid sagging. Depending on the type of system — two-hydrofoil system or the four-hydrofoil system — the exoskeleton can be modified to use one slat or two slats respectively. Commercially available reconfigurable aluminum components are extensively used to make critical joints and attachments. The slats have been pre-drilled to match the standard pattern of the aluminum components.

The hydrofoil paddles were 3-D printed using PLA and attached to the servo motors via 1/4"×3" shafts and matching couplings. The hydrofoil measures 4" in chord length, 4" in span length and 0.11" inches in thickness. The pitching of the hydrofoils is controlled by Hi-tech 5665MH high torque servo motors.

The electronics module consists of a Particle Photon 120 MHz micro-controller. The controller is equipped with an XBee for serial communication with a PC. The electronics are powered by an on-board 6V 2200mAh NiMH battery pack placed beneath the circuit. An added feature to this circuit is the current sensor module, which measures the current flowing into the servomotors by connecting a shunt resistor (0.01Ω) in series and measuring the voltage across it. To eliminate white noise, we apply a second order RC filter over the voltage measurement. The Photon stores the voltage measurement data into an SD card at a sampling rate of 500Hz. Using the calibration data of the current sensor, we measure the current flowing through the servos during the pitching motion of the hydrofoils.

In order to quantify the propulsive efficiency, we consider that the drag force is equivalent to the net thrust/cycle averaged force F_x of the system when it reaches steady state. To measure the drag forces experienced by the swimmer, we deploy the swimmer in a closed-loop, free-surface water channel with a test section 1m wide, 2m long and 1m deep. We use a high precision load cell in conjunction with a MyDAQ data acquisition device and an AD623 instrumentation amplifier to measure the drag experienced by the swimmer. The flow in the water channel is set to different speeds and force measurements are recorded keeping the hydrofoils fixed in the direction of the background flow. The top image in Figure 4.4 shows the swimmer being deployed in the water channel and rigidly mounted to the fixed aluminum beam on the surface. The plot obtained for the drag force is then approximated to a parabolic fit shown in the bottom image in Figure 4.4 which is used to calculate the drag force for any swimming speed.

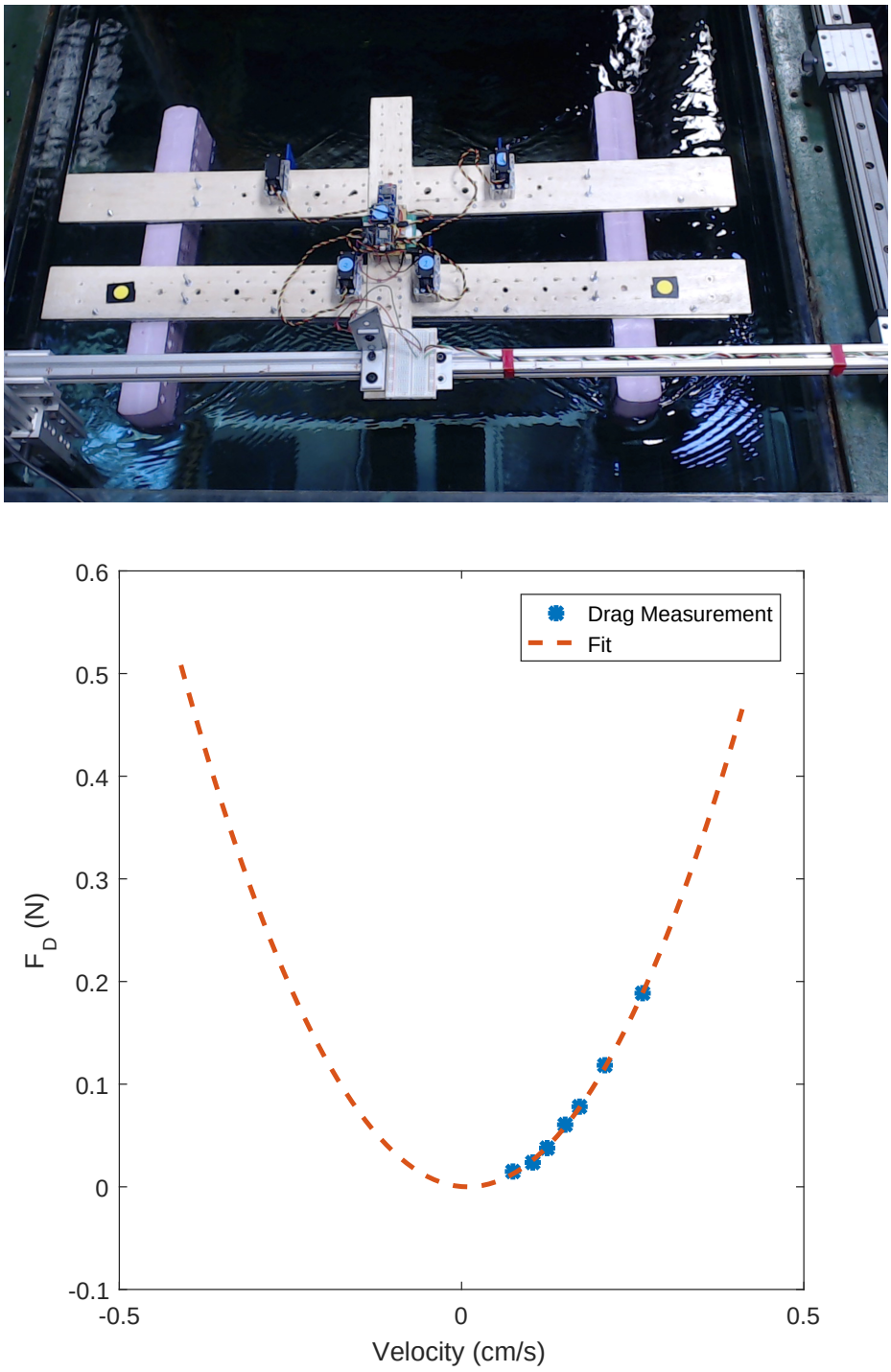

Figure 4.4: Drag force measurement setup and calibration graph.

Figure 4.5 depicts the experimental test pool which is 4ft wide, 8ft long and 6" deep. A Raspberry pi setup with a VGA camera is mounted directly above the test

pool. Four stationary markers have been positioned at 4 distinct locations on the periphery of the pool. These serve as reference markers for motion tracking analysis. The exoskeleton has two brightly colored markers, seen in yellow in Figure 4.6. We apply a projective transformation on the image frames with the aid of the reference markers to obtain the coordinates of the markers on the exoskeleton. Figure 4.7 shows the trajectories overlapped on the four-hydrofoil swimmer in the test pool.

4.1.1 Two-hydrofoil swimmer: experimental procedure

For the two-hydrofoil swimmer (Fig. 4.6), we deploy two servo motors on a single slat and vary the lateral separation between them in multiples of chord length C in the range of $C, 2C$ and $3C$. We set the frequency to f=0.5Hz and amplitude to $\theta_0 = \pi/6$ radians for our experiments. As mentioned in chapter 4, the two hydrofoils oscillate with a phase difference of π with respect to one another. The position data is collected from the Raspberry Pi in the form of a video in addition to the power consumption data being logged into an SD card on the on-board electronics module.

4.1.2 Four-hydrofoil swimmer: experimental procedure

The exoskeleton of the four-hydrofoil swimmer employs two slats that seat four servo motors as shown in Figure 4.6. Each row has two servomotors with lateral separation between motors in the same row varied in multiples of chord length C. The longitudinal separation between the trailing edge of the front row(FR) hydrofoils and the leading edge of the back row(BR) hydrofoils is also varied in multiples of hydrofoil chord length C. In total, 540 experiments were performed by fixing the pitching frequency at $f = 0.5$Hz and θ_0 to $\pi/6$ radians and varying the following parameters: phase differential ϕ ($-5\pi/6 \leq \phi \leq \pi$ in increments of $\pi/6$) between the FR and BR hydrofoils, longitudinal spacings ($0.5C$, C and $2C$) and lateral spacings (C, $2C$, $3C$ and $6C$ for both the FR and BR).

4.2 Results and discussions

4.2.1 Variation of lateral spacing in the two-hydrofoil system

Figure 4.8 shows a plot of the translation of the two-hydrofoil swimmer system. We find that the thrust augmentation is greater in the case of one-chord length lateral spacing which shows a 10% increase for the this configuration. This strengthens the notion about the effect of peristaltic pumping [15] in the space between the two hydrofoils. We conjecture the wake dynamics with this effect in Figure 4.9. Vortices shed during the first half of each cycle are denoted by 1. The other half vortices are denoted by 2. The vortices shed in the wake of the swimmers in each half cycle interact with oppositely signed vortices and pair up to create energetic momentum jets. These momentum jets jettison energy to the flow and augment the thrust production of the swimmer based on Newton's third law. Also, due to the out-of-phase relationship between the pitching action of the two hydrofoils, each foil induces a lateral velocity that increases the effective angle of attack of the other foil, thereby increasing bound circulation which in turn leads to thrust enhancement in the closely spaced configuration [15]. At larger spacing arrangements, this effect diminishes and the thrust is subtly affected by changes in vortex shedding.

Power consumption data (Figure 4.10) reveals that the cycle averaged power consumption P for the one chord length spacing was 0.8 times that of the two-chord length spacing case and 0.87 times that of the three chord length spacing. The propulsive efficiency η was found to be the best for the one-chord length configuration with an increase of up to 2.7 times compared with the worst performing two-chord length configuration. This decrease in propulsive efficiency dramatizes the dominance of the vortex interactions in the closely spaced lateral spacings and is mostly attributed to the jet effect.

4.2.2 Variation of lateral and longitudinal spacing in the four-hydrofoil system

The velocity data obtained for the four-hydrofoil hydrodynamic swimmer is shown in Figure 4.11. Each dot represents the velocity of a particular configuration. For example- a lateral configuration pair of '$C, 2C$' represents one-chord length lateral spacing in the front row (FR) and two-chord lengths in the back row (BR). The separation between the trailing edge of the FR hydrofoils and the leading edge of the BR hydrofoils is represented as the longitudinal spacings/configurations and ϕ is the phase difference between the FR and the BR hydrofoil pitching motions.

The phase difference(ϕ) in Figure 4.11 is listed for values between $-5\pi/6$ and π in steps of $\pi/6$ radians and wraps around owing to symmetry. It is observed from Figure 4.11 that for longitudinal configuration of half- and one-chordlendths, the system is able to achieve greater speeds for phase differences in the vicinity of π radians.

The configurations with six chord lengths in any possible spacing combinations are nonreactive to any meaningful vortex interactions due to the distant spacing and serve as benchmarks for the propulsive efficiency comparisons.

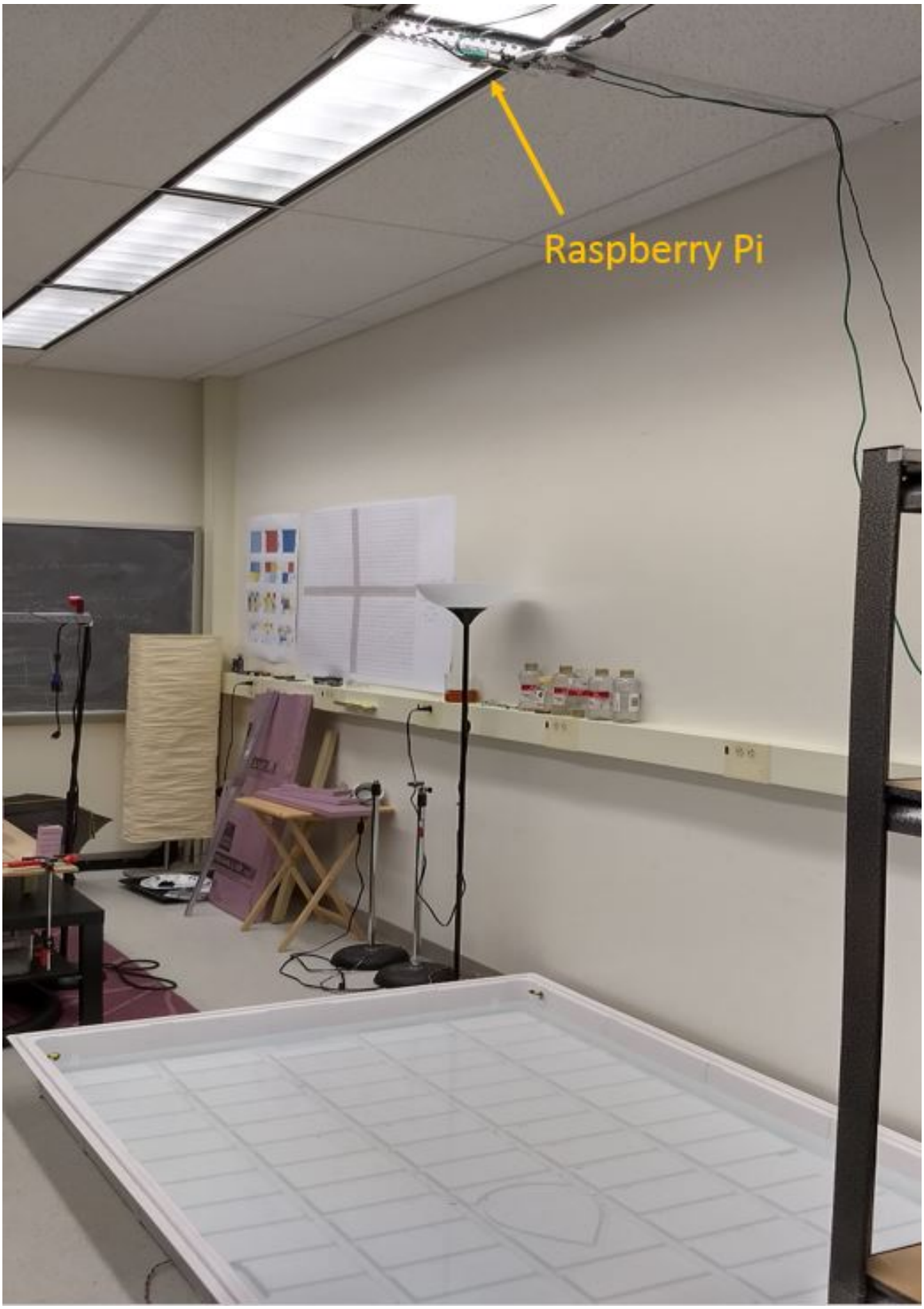

Figure 4.5: Pool test section with the Raspberry Pi mounted over it.

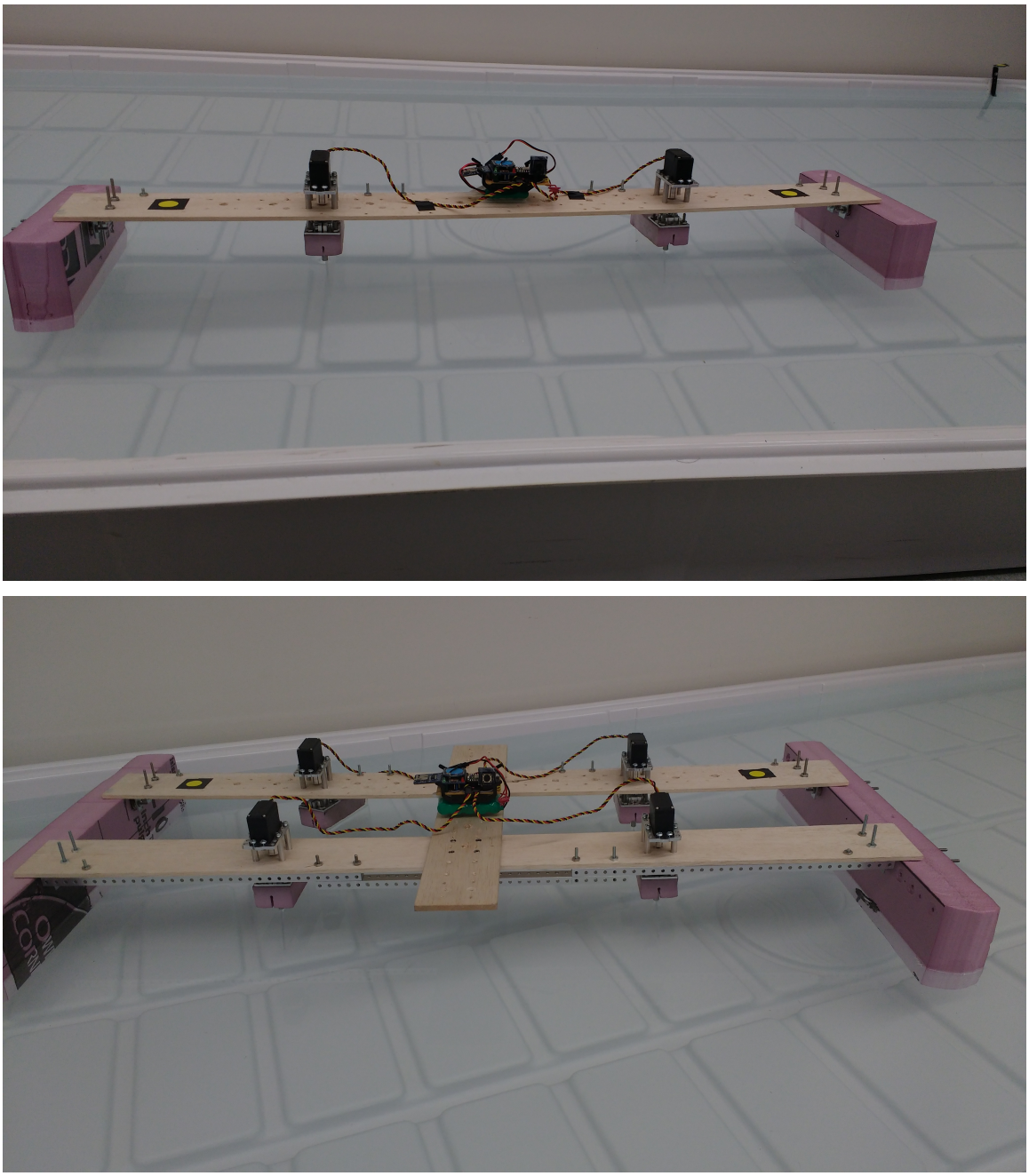

Figure 4.6: Experimental two-hydrofoil and four-hydrofoil swimmers.

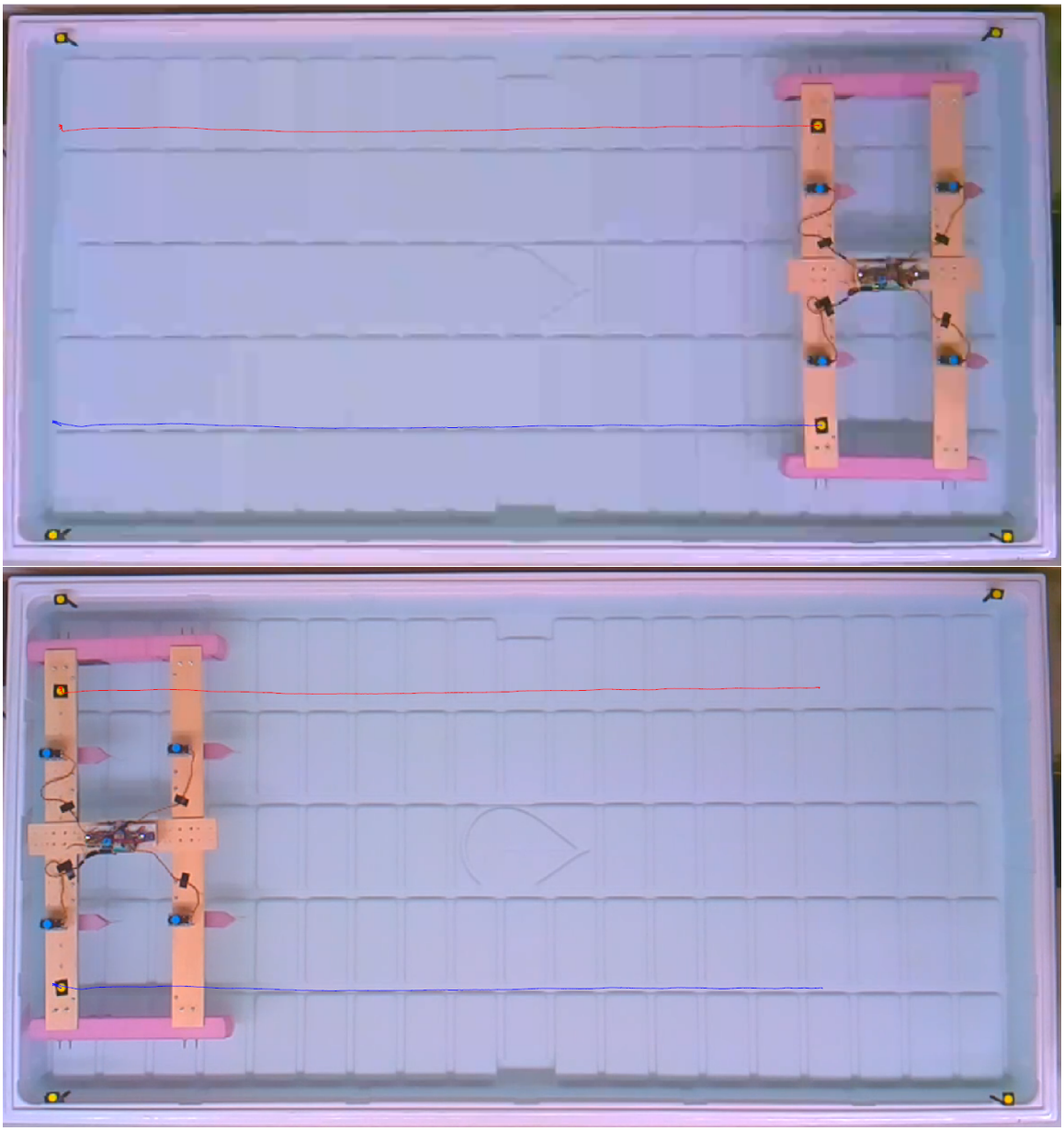

Figure 4.7: Trajectory information overlayed on the four-hydrofoil swimmer.

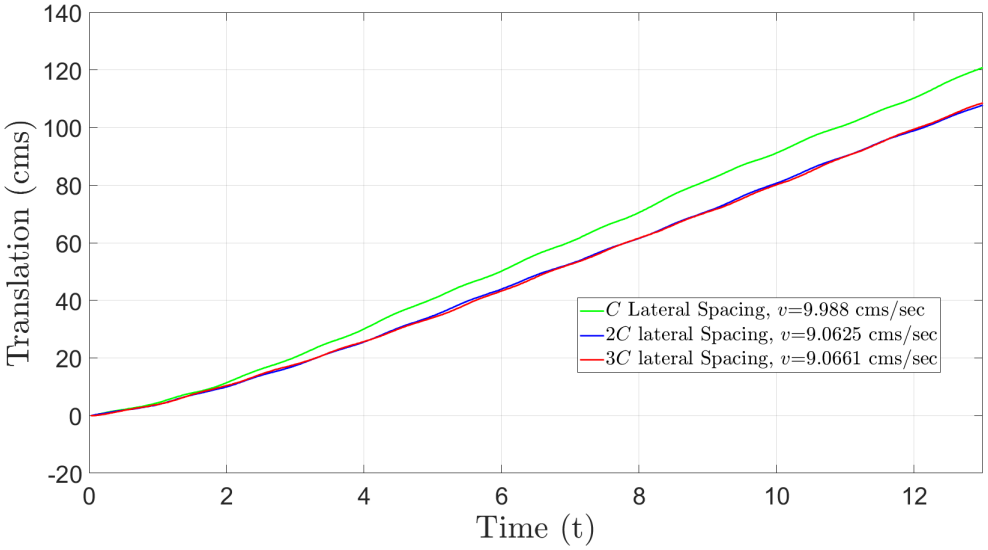

Figure 4.8: Comparison for different lateral spacing configurations in the two-hydrofoil swimmer.

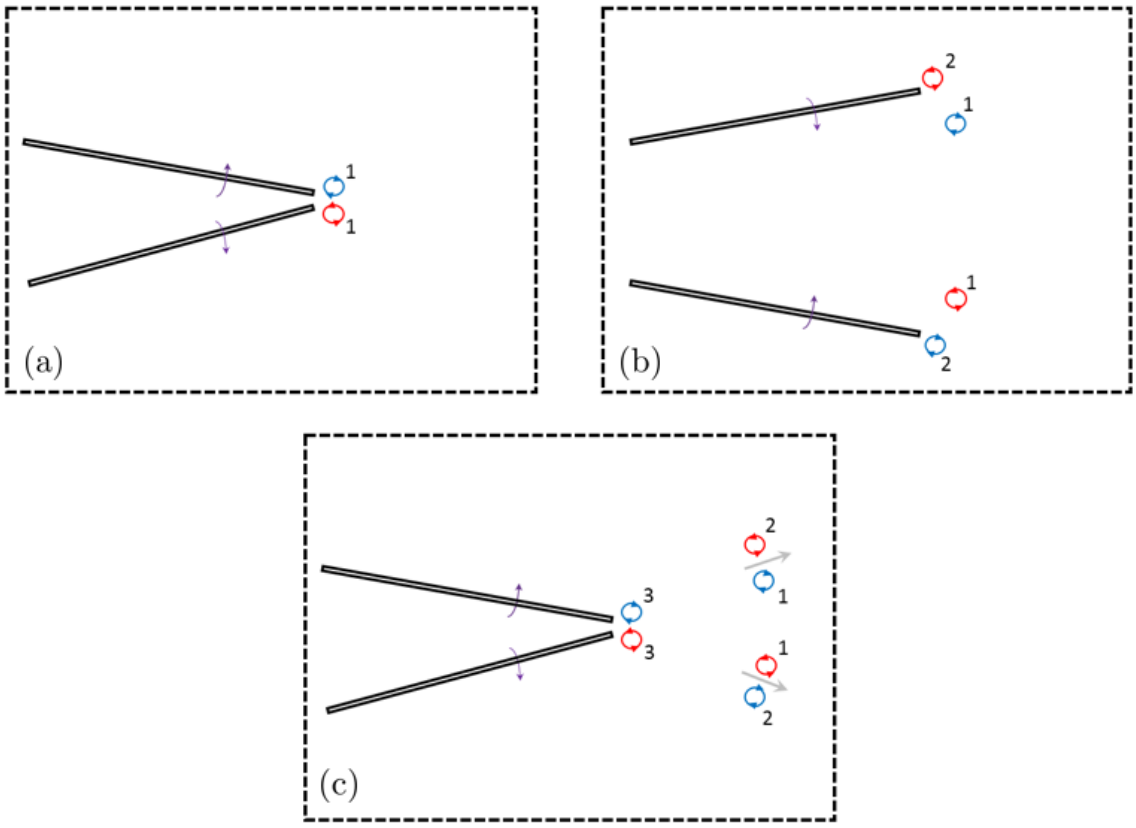

Figure 4.9: Creation of momentum jets in the wake of the hydrofoils. The clockwise vortices are represented in blue and counter-clockwise in red.

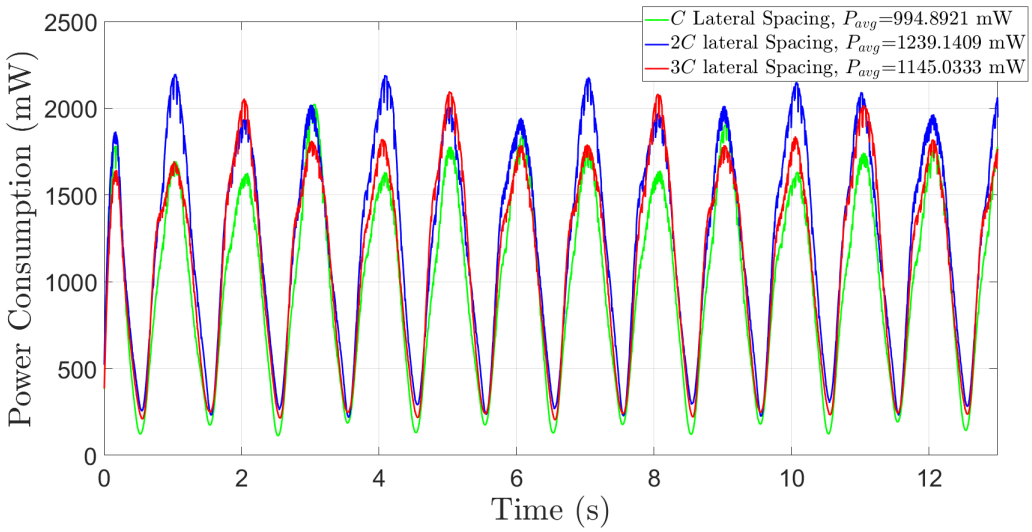

Figure 4.10: Two paddle swimmer power consumption graph.

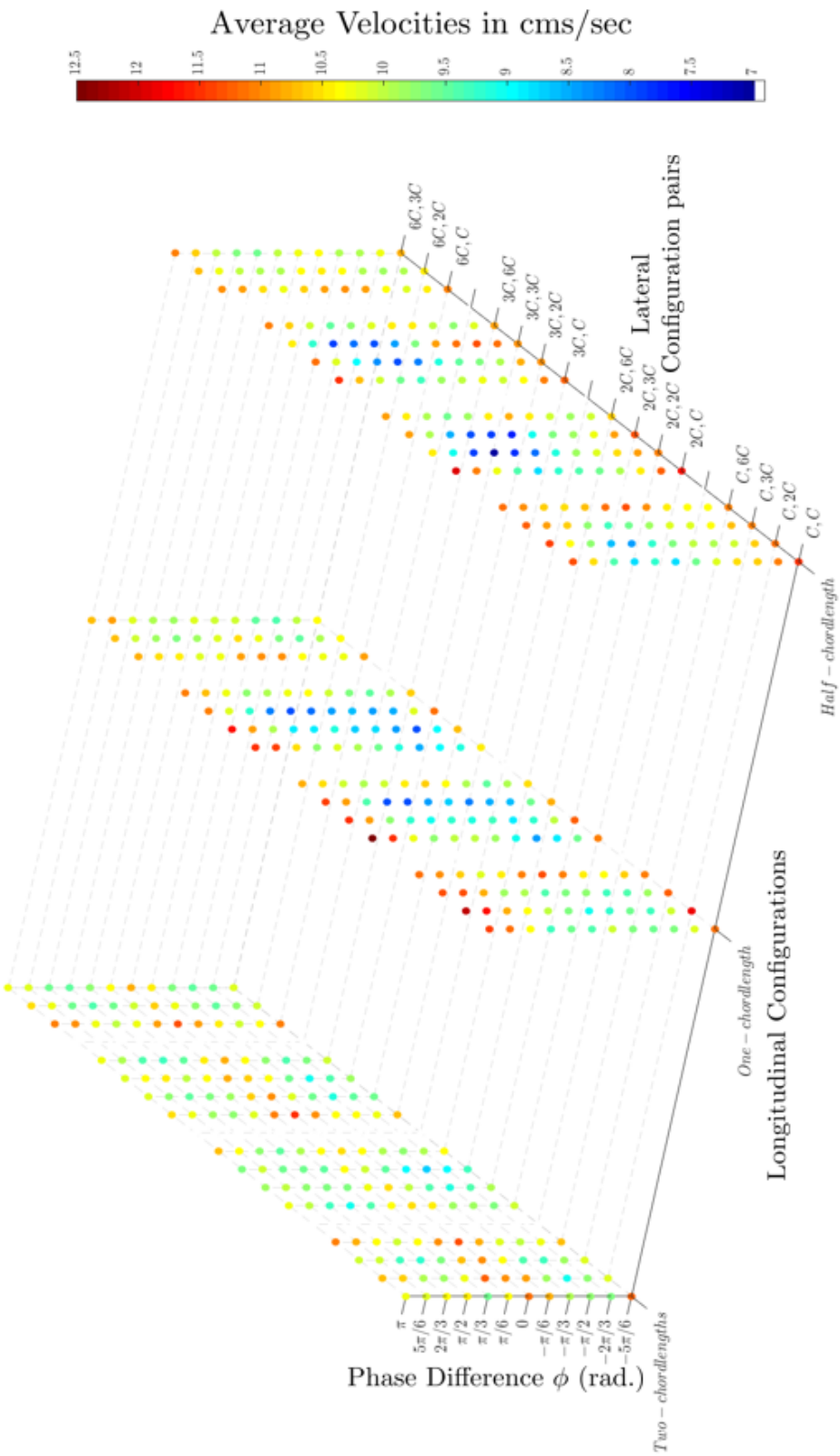

Figure 4.11: Cycle averaged velocity data for the four-hydrofoil system. Each dot represents the velocity of a particular configuration. For example- a lateral configuration pair of $C, 2C$ represents one-chord lengths of lateral spacing in the front row (FR) and two-chord lengths in the back row (BR). The separation between the FR and BR is given by the longitudinal spacings/configurations and ϕ is the phase difference between the FR and the BR.

The velocities in the half- and one- chord length longitudinal spacings, represented by the first two sections of dots from the right in Figure 4.11, gave the highest and lowest velocities depending on the phase differential ϕ. To understand this behavior, we make the claim that a body oscillating within the wake of a reverse von Kármán vortex street of a preceding hydrofoil will experience less or more thrust benefit depending on the phasing between the two bodies and the formation of opposite polarity vortex pairs that are responsible for thrust augmentation. This is analogous to the discovery of Beal et. al. [25], where a steady flow across a bluff body results in the entrainment of a von Kármán vortex street and when an undulating deceased trout is placed within the wake of the vortex street, the body of the trout senses the pressure variations of the spinning eddies and undulates in a particular fashion such that the vortices shed by the undulation of the trout pair up with the oncoming counter-rotating vortices to generate highly energetic momentum jets. This enables the dead trout to extract energy and propagate against the flow and towards the bluff body.

Figure 4.12 shows the trend in velocities for the three longitudinal spacings considered across all measured phase differences leaving out the minimal vortex interaction pairs($6C$ lateral spacing in either FR or BR). It is observed that for the one-chord length longitudinal spacing, the velocity trend decreases and reaches a minimum near the left side of zero ϕ, and then increases as $\phi \to \pi$ radians. For the half-chord length case, this trend is shifted to the right of zero ϕ depicting a minimum on the right and then increases as $\phi \to \pi$ radians. Contrastingly, the two-chord length case resembles a harmonic function, where the velocity initially is at a maximum at $\phi = -\pi$, then decreases as ϕ is increased and reaches a local minimum at $-\pi/2$, after which it advances upwards to reach a local maximum at zero ϕ. This behavior is mirrored on the right side of zero as $\phi \to \pi$. Vortices shed from the trailing edge of the FR paddles interact constructively or destructively to display significant performance shifts.

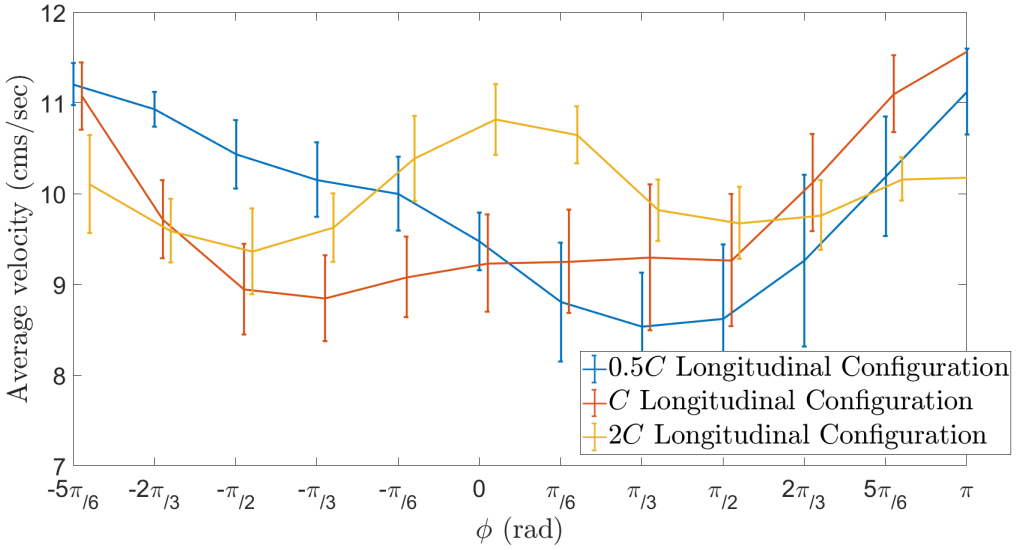

Figure 4.12: Velocity trend lines for various longitudinal configurations with respect to the phase difference between the FR and BR. The vertical lines represent the range of velocities for every lateral spacing pair excluding the $6C$ lateral configurations pairs(minimal vortex interaction pairs) in either FR or BR.

But, in the two-chordlength longitudinal configurations, it is observed that these vortices loose considerable strength before they reach the hydrofoils in the BR owing to minimal vortex interactions.

We compare this behavior of the longitudinal two-chord length configuration with that of the ones assumed to have minimal vortex interactions (configurations with $6C$ lateral spacing) shown in Figure 4.13. The trends display local maxima at $\phi \to 0$ and $\phi \to \pi$ for these configurations. We make the assertion that the connectivity of the hydrofoils via the exoskeleton is responsible for this behavior. At ϕ=0, all the hydrofoils move in unison, reaching the peak amplitude θ_0 at the same instant. This causes a net thrust in the system, and the system as a whole benefits from this phasing. On the contrary, a phase difference of $\phi = -\pi/2$ or $\phi = \pi/2$ does not produce the same amount net force at any particular instant due to asynchronicity. However, a phase difference of $\phi = \pi$ enables the paddles to produce net thrust as the sweep angle of the hydrofoils reaches the absolute maximum at the same instant.

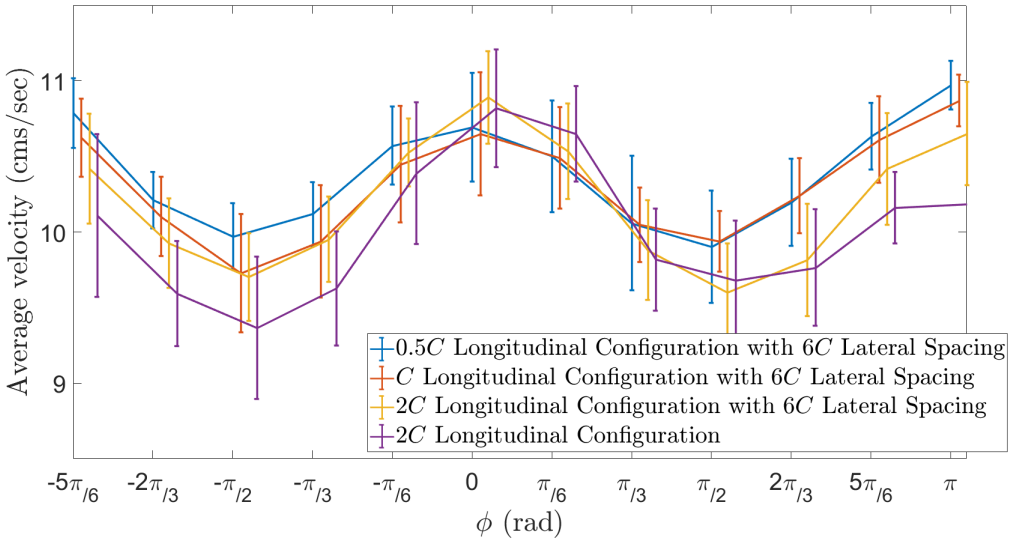

Figure 4.13: Velocity trend lines for configuration pairs assumed to have minimal vortex interactions.

To compare the differences in propulsive efficacy η, we normalize the efficiency with respect to a configuration that has no hydrofoils in the FR and two hydrofoils in the BR and placed one-chord length apart laterally in order to negate the performance benefit from the effect of peristaltic pumping [15] and to only accommodate for vortex interaction behaviors between the front and back hydrofoils. We denote the normalized propulsive efficiency as η^*.

The normalized efficiencies were found to be the lowest for configurations that had hydrofoils separated laterally by two or three-chord lengths in the FR and BR. This is evident from the dark blue dots seen in Figure 4.14 in the lateral configuration pairs given by -'$2C, 2C$', '$2C, 3C$', '$3C, 2C$', '$3C, 3C$', and for ϕ values enclosing zero and its surroundings. Depending on the phase difference ϕ, the vortices shed by the trailing edge of the FR hydrofoil interacts constructively or destructively with the vortices formed at the leading edge[1] of the BR hydrofoil. We have seen in Section 4.2.1 that positively signed vortices pair up with their negative counterparts to inject

[1]A leading edge vortex is formed due to flow separation and creates a low suction region on the periphery of the hydrofoil during the pitching motion.

momentum jets to increase thrust production. We consider these kind of vortex interactions to be constructive and these contribute to thrust augmentation whereas vortex pairs containing vortices of the same sign give rise to bigger single polarity vortices which then advect into the wake away from the centerline, causing thrust deterioration. These interactions are considered to be destructive.

The largest increase in propulsive performance was noticed in the 'C, C' lateral spacing pair with one-chord length of longitudinal spacing. Although, this configuration did not achieve the highest thrust(as seen on Figure 4.11) compared with other configurations(the '$2C, C$' lateral configuration pair with one-chord length longitudinal spacing and $\phi = \pi$ had the highest average velocity), the power consumed by the pitching action of the servo motors was found to be around 30% less compared to the configurations that produced higher thrust. Boschitsch et al. [17] discussed about the possibility of formation of a low pressure region at the leading edge of the downstream foil being detrimental to the thrust production in the upstream foil at closely spaced configurations which is seen here as well. This behavior supplements our belief that the tightly spaced configuration of half-chord length longitudinal spacing and one-chord length lateral spacing in the FR and BR represented by 'C, C', which is the most tightly spaced configuration in our case, does not lead not the best propulsive efficacy.

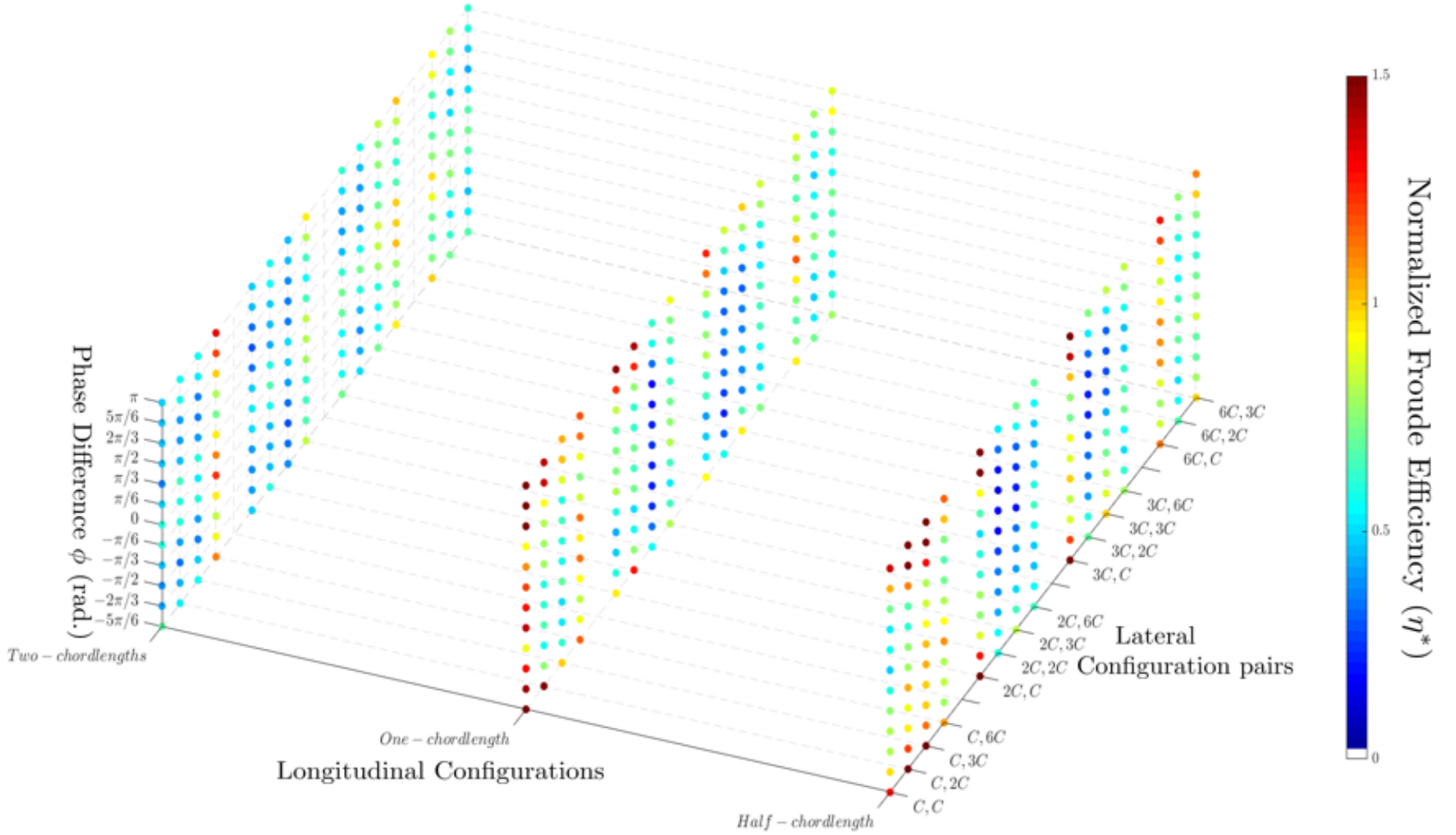

Figure 4.14: Normalized Froude Efficiencies η^*. Each dot represents the efficiency of a particular configuration. For example- a lateral configuration pair of $C, 2C$ represents one-chord lengths of lateral spacing in the front row (FR) and two-chord lengths in the back row (BR). The separation between the FR and BR is given by the longitudinal spacings/configurations and ϕ is the phase difference between the FR and the BR.

4.2.3 Comparison of sinusoidal and two-mode frequency gait

It is hypothesized in literature that gaits with non-smooth motions can generate greater propulsive benefits over smooth sinusoids. Floryan et al.[26] demonstrated the energetic advantages of intermittent non-smooth swimming over continuous motions.

The simplest choice for selecting such an intermittent gait is by the superposition of the multiple frequencies. We consider a gait with the superposition of two frequencies — a first-mode frequency f and second-mode frequency $2f$ — and name it as the *two-mode frequency gait*. Using the same physical two-hydrofoil swimmer system, we prescribe this gait as the actuation signal for the hydrofoils where

$$\theta = \theta_0 sin(\omega t) + \lambda\theta_0 sin(2\omega t + \phi). \tag{4.5}$$

ϕ is the phase difference and $\lambda \in [0, 1]$ is the ratio of second mode amplitude to first mode amplitude and can also be termed as the smoothing factor. This value of λ characterizes the pitching of the hydrofoil as either intermittent or continuous. We set the frequency f at 0.5Hz and amplitude θ_0 to $\pi/10$ to avoid large flow separation. We switch from continuous to intermittent by defining $\lambda = 0.5$ and vary the phase ϕ between 0 and π.

The comparison of translation of the two-hydrofoil swimmer employing the two-mode frequency gait and the sinusoidal gait is shown in Figure 4.16. It is seen that for all lateral spacing arrangements that the two-mode frequency gaits generate more thrust than the sinusoidally pitching hydrofoils. On an average, thrust enhancements of upto 20% were noticed.

To support our findings and to compute the flow characteristics, we perform simulations using panel methods assuming inviscid, incompressible flow[2]. Figure 4.17 depicts that the wake structure for the two-mode frequency gait, with its central sheet of vorticity sandwiched between pairs of vortex cores, looks qualitatively differ-

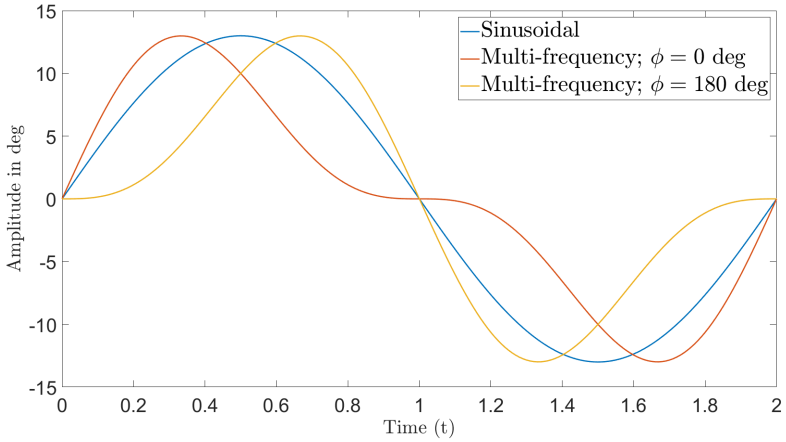

Figure 4.15: Sinusoidal and the two-mode frequency actuation signals; λ=0.5.

ent than for the regular sinusoidal case which has a simpler 2S wake structure. We conjecture that the two-mode frequency wake exhibits more jet flow than the sinusoidal wake, which accounts for the improved thrust performance via Newton's third law.

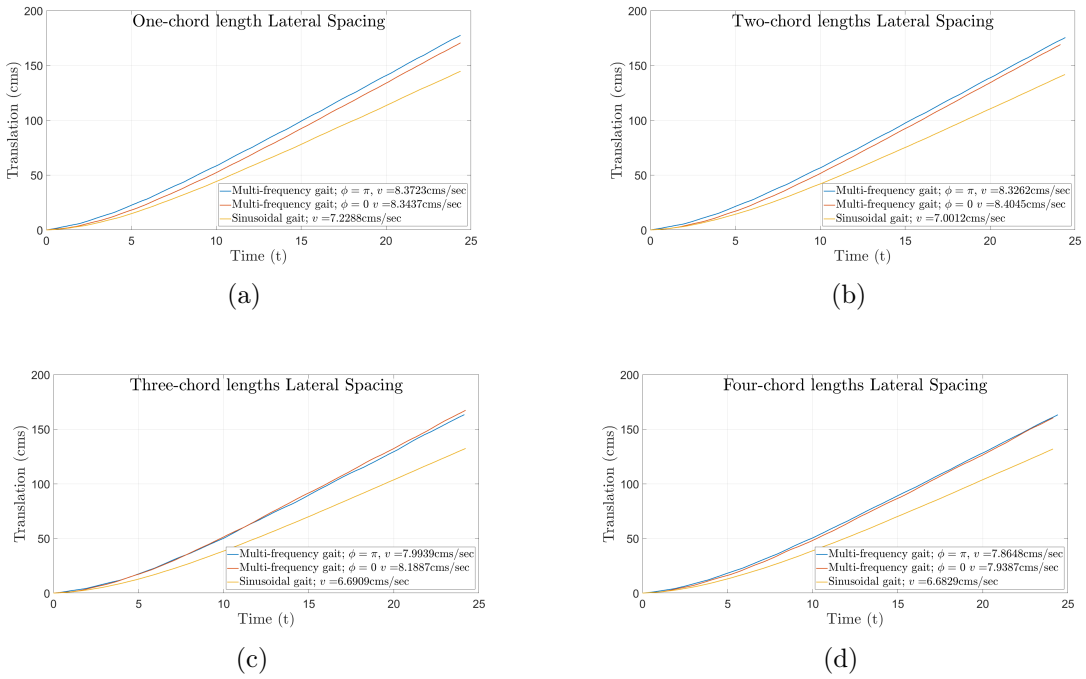

Figure 4.16: Experimental comparison of sinusoidal and two-mode frequency gaits.

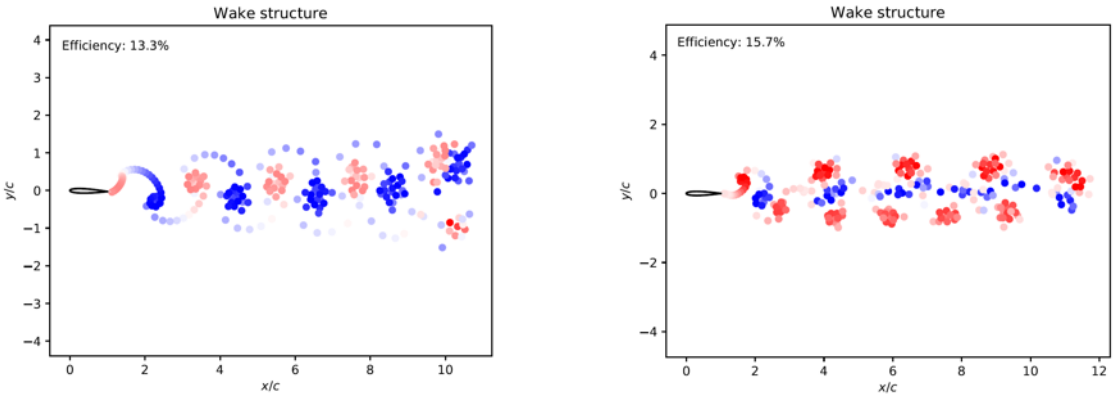

Figure 4.17: Wake structure predicted by the panel method solver for unsteady 2D flow[2]. *Left*: Wake structure of the sinusoidal gait *Right*: Wake structure of the two-mode frequency gait

CHAPTER 5: CONCLUSIONS AND FUTURE WORK

We geometrically analyzed two systems — the Purcell three-link swimmer (explained in Section 2.1) and a four-paddle system (explained in Section 2.2) — in low Reynolds number flow. The purpose of performing this in a low Reynolds number fluid was to make the assumption that the paddles are completely decoupled hydrodynamically and that the principal connection A can be computed for using slender-body theory. In doing so, we have not only validated our model for locomotion at low Reynolds number but have also shown that when the physics underlying a control system justify a model based on a principal connection, a limited sampling of the system's responsiveness to select inputs can be used to estimate the curvature of this connection, from which the system's response to an arbitrary periodic input can then be estimated in the absence of a theoretical model[1].

The analytical and experimental plots for the three-link Purcell swimmer are shown in Figure 2.12, and for the four-paddle swimmer in Figure 2.13. The holonomy, as calculated by experimental data, show identical features with the analytically computed local curvatures considering minor irregularities which may be due to the assumptions made in the theoretical model and uncontrollable experimental conditions.

In chapter 3, we use reinforcement learning to identify the optimal sequence of piecewise constant control actions for the four-paddle swimmer in low Reynolds number flow. The reinforcement learning results indicate that the optimal way to achieve translation of the four-paddle system with non-holonomic constraints over long timescales is to perform cyclic actuation that exploits curvature according to the geometric theory — and that exploits the nontrivial topology of the manifold of internal robot shapes — while optimal locomotion over short times scales requires adaptation for

different initial conditions.

In the context of high Reynolds number regime flow, there exists shortcomings in the field of geometric mechanics to study the hydrodynamic interactions due to viscous vortex shedding. We base our research to the experimental side and leave out the model based analysis for future work.

Based on our experimental results of hydrodynamic coupling among multi-hydrofoil systems, we propose to optimize the spatial arrangement of paddles to maximize thrust or propulsive efficiency. The results obtained for the two hydrodynamic systems are consistent with some of the literature, but the exactness depends upon replicating all the conditions such as hydrofoil dimensions, Reynolds number and many others. The literature also talks about keeping a constant Strouhal numbers[1] [18], [17] for experiments, but we do not refer to Strouhal numbers because of a major difference being that the experiments were conducted in a free-swimming environment without any background flow. The Strouhal number for our system keeps changing with change in swimming speed. Our study of these systems enables us to pose this as an optimization problem with the goal of finding the energetically efficient arrangement of cooperatively pitching hydrofoils.

We find that the dynamics of vortex interactions are dominant when hydrofoils are placed in close arrangements. Our experimental data predicted maximum efficiency for the lateral spacing of one-chord length for the two-hydrofoil swimmer, and longitudinal spacing of one-chord length in conjunction with the lateral spacing pair 'C, C' for the four-hydrofoil swimmer with an out-of-phase pitching relationship between the front row and the back row hydrofoils. These results demonstrate the importance of geometrical spacing and phasing in the study network synchronization of swimmers.

[1]Strouhal number is a dimensionless number and is defined as the ratio of the product of the vortex shedding frequency and the characteristic chord length to the free stream velocity or swimming speed given by $St = \frac{fC}{u_\infty}$.

5.1 Future Work

The ground for performing analysis in low Reynolds number is that the system can be considered driftless and there exists no hydrodynamic coupling among the hydrofoils. We propose to come up with a geometric model underlying systems with hydrodynamic drift which can be used to model for behavior of these systems in any given fluid regime.

Passive bodies in the wake of preceding swimmers and actuated by stiffness springs can increase the propulsive efficiency of the system as a whole in the context of the high Reynolds number systems. We hope to study these systems and make useful inferences.

We did not consider turning gaits for our system due to space constraints of our test pool section. In the future, we hope to characterize these gaits as well.

We briefly summarize about trajectory optimization using a very simple and naive reinforcement learning technique. More complex techniques in RL involve the application of function approximators like artificial neural networks. It will be interesting to deploy these algorithms in real-time on the robotic setup.

Discrete differential geometry coupled with deep reinforcement learning, a model-free control technique for mechanical systems, may offer elegant mathematical conjectures that may not be well-defined by geometric mechanics alone. Exploring these mathematical conjectures to use them as tools for motion planning and navigation poses an interesting challenge.

REFERENCES

[1] R. Abrajan-Guerrero, R. Bhansali, and S. D. Kelly, "Using physical experiments to estimate the curvatures of principal connections underlying swimming at low reynolds number," in *Control Conference (ASCC), 2017 11th Asian*, pp. 1314–1319, IEEE, 2017.

[2] M. Fairchild, "Unsteady boundary element method 2d." `https://github.com/mjfairch/ubem2d_matlab`.

[3] E. Muybridge, *Animal Locomotion: An Electro-photographic Investigation of Consecutive Phases of Animal Movements, 1872-1885: 112 Plates*. Published under the auspices of the University of Pennsylvania, 1887.

[4] J. Gray, "Studies in animal locomotion," *Journal of experimental biology*, vol. 10, no. 1, pp. 88–104, 1933.

[5] D. F. Hoyt and C. R. Taylor, "Gait and the energetics of locomotion in horses," *Nature*, vol. 292, no. 5820, pp. 239–240, 1981.

[6] E. M. Purcell, "Life at low reynolds number," *American journal of physics*, vol. 45, no. 1, pp. 3–11, 1977.

[7] A. Shapere and F. Wilczek, "Geometry of self-propulsion at low reynolds number," *Journal of Fluid Mechanics*, vol. 198, pp. 557–585, 1989.

[8] R. M. Murray and S. S. Sastry, "Nonholonomic motion planning: Steering using sinusoids," *IEEE Transactions on Automatic Control*, vol. 38, no. 5, pp. 700–716, 1993.

[9] S. D. Kelly and R. M. Murray, "The geometry and control of dissipative systems," in *Decision and Control, 1996., Proceedings of the 35th IEEE Conference on*, vol. 1, pp. 981–986, IEEE, 1996.

[10] J. M. Anderson, "Vorticity control for efficient propulsion.," tech. rep., MASSACHUSETTS INST OF TECH CAMBRIDGE, 1996.

[11] R. Gopalkrishnan, M. Triantafyllou, G. Triantafyllou, and D. Barrett, "Active vorticity control in a shear flow using a flapping foil," *Journal of Fluid Mechanics*, vol. 274, pp. 1–21, 1994.

[12] F. Fish and G. Lauder, "Passive and active flow control by swimming fishes and mammals," *Annu. Rev. Fluid Mech.*, vol. 38, pp. 193–224, 2006.

[13] M. S. Triantafyllou, G. Triantafyllou, and D. Yue, "Hydrodynamics of fishlike swimming," *Annual review of fluid mechanics*, vol. 32, no. 1, pp. 33–53, 2000.

[14] D. Weihs, "Hydromechanics of fish schooling," *Nature*, vol. 241, no. 5387, pp. 290–291, 1973.

[15] L. J. Zhang and J. D. Eldredge, "Hydrodynamics of undulatory fish schooling in lateral configurations," *arXiv preprint arXiv:1003.4441*, 2010.

[16] S. D. Kelly and H. Xiong, "Controlled hydrodynamic interactions in schooling aquatic locomotion," in *Decision and Control, 2005 and 2005 European Control Conference. CDC-ECC'05. 44th IEEE Conference on*, pp. 3904–3910, IEEE, 2005.

[17] B. M. Boschitsch, P. A. Dewey, and A. J. Smits, "Propulsive performance of unsteady tandem hydrofoils in an in-line configuration," *Physics of Fluids*, vol. 26, no. 5, p. 051901, 2014.

[18] P. A. Dewey, D. B. Quinn, B. M. Boschitsch, and A. J. Smits, "Propulsive performance of unsteady tandem hydrofoils in a side-by-side configuration," *Physics of Fluids*, vol. 26, no. 4, p. 041903, 2014.

[19] R. S. Sutton and A. G. Barto, *Reinforcement learning: An introduction*, vol. 1. MIT press Cambridge, 1998.

[20] R. L. Hatton and H. Choset, "Geometric swimming at low and high reynolds numbers," *IEEE Transactions on Robotics*, vol. 29, no. 3, pp. 615–624, 2013.

[21] R. Cox, "The motion of long slender bodies in a viscous fluid part 1. general theory," *Journal of Fluid mechanics*, vol. 44, no. 4, pp. 791–810, 1970.

[22] Wikipedia, "Markov decision process — wikipedia, the free encyclopedia," 2017. [Online; accessed 18-November-2017].

[23] L. Busoniu, R. Babuska, B. De Schutter, and D. Ernst, *Reinforcement learning and dynamic programming using function approximators*, vol. 39. CRC press, 2010.

[24] V. Mnih, K. Kavukcuoglu, D. Silver, A. Graves, I. Antonoglou, D. Wierstra, and M. Riedmiller, "Playing atari with deep reinforcement learning," *arXiv preprint arXiv:1312.5602*, 2013.

[25] D. Beal, F. Hover, M. Triantafyllou, J. Liao, and G. Lauder, "Passive propulsion in vortex wakes," *Journal of Fluid Mechanics*, vol. 549, pp. 385–402, 2006.

[26] D. Floryan, T. Van Buren, and A. J. Smits, "Forces and energetics of intermittent swimming," *arXiv preprint arXiv:1703.00971*, 2017.